Impact Robustness vs. Torque Bandwidth: A Design Guide for Differential Elastic Actuators

Anton Shu[1,2], Clara Raschel[2], Manuel Keppler[2], Armin Wedler[2], Martin Görner[2]

***Abstract*—Differential Elastic Actuators (DEAs) connect a motor and a spring via differential gears to a shared output shaft, offering a more compact solution for creating mechanically robust systems than Series Elastic Actuators (SEAs), with superior torque transmission at high frequencies. The key to maximizing DEA performance lies in the careful selection of stiffness, inertia, and damping values to meet specific requirements for performance and durability. We introduce a DEA design guide that utilizes open-loop torque-bandwidth for performance evaluation and the magnitude of impact-induced gear torque for robustness evaluation. This approach enables determining DEA parameters using closed-form equations, eliminating the need for simulations or extensive expert knowledge. The effectiveness of our method is confirmed through experiments with a re-configurable DEA prototype.**

***Index Terms*—Compliant Joint/Mechanism, Mechanism Design, Compliance and Impedance Control, Differential Elastic Actuator**

I. Introduction

Today, there is a growing number of humanoids, quadrupeds and wheeled-legged robots that target a large variety of real-world applications. In logistics, industrial plant inspection or planetary exploration, these robots operate in uncontrolled and partially unknown environments where they experience intentional and unintentional impacts, as shown on the top left of Fig. 1. This requires inherently robust hardware and actuators that mitigate impacts while providing sufficient torque bandwidth for smooth interaction control. Due to their robust mechanical structure, torque-controlled elastic actuators have become a favorable choice for such applications [1]–[5]. However, their robustness to impacts usually comes at the price of decreased open-loop torque bandwidth [6] and thus limited performance [7]. Therefore, it is crucial that robot designers know how to properly parameterize an elastic actuator in order to find a good trade-off in between performance and robustness.

Since Pratt et al. introduced their original Series Elastic Actuator (SEA) in 1995 [8], many compliant actuators designs have been presented. These can be categorized in groups based on spring placement and the resulting force-flow [9] as, SEAs [10]–[12], Parallel Elastic Actuators (PEAs) [13], [14] and Differential Elastic Actuators (DEAs) [15]–[19]. In contrast to SEAs and PEAs, DEAs use a differential gear as shown in Fig. 1, where one shaft is connected to the motor, one to the spring and one to the link. This allows for very compact, high torque density designs, as analyzed in [18], which is a desirable actuator property in general purpose robotic systems.

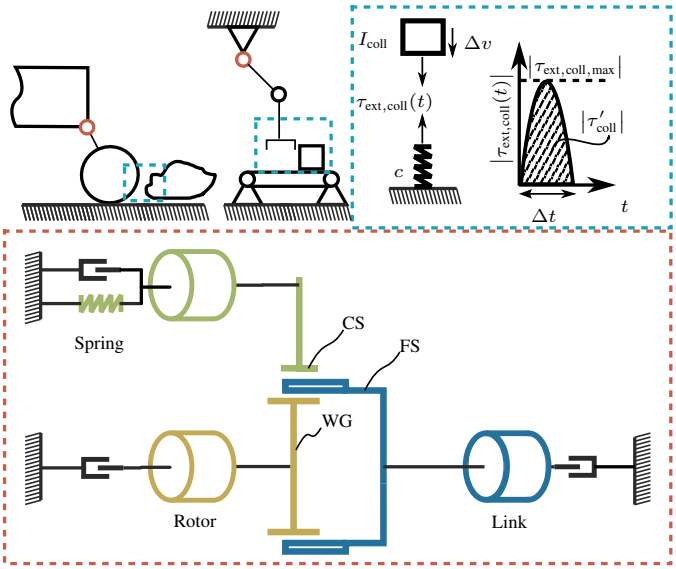

Fig. 1. A Differential Elastic Actuator (DEA) shown in red is used to actuate a multi-link kinematics (Top Left). The actuator is subject to application-specific torque bandwidth and impact robustness requirements. To select the mechanical parameters of spring, rotor and gearbox of the DEA we use a spring-mass impact model (Top Right) and a second-order model of the DEA to derive a design guideline. **Top Left**: A DEA shown in red is used to actuate a multi-link kinematics. Within the environment it collides with a different multi-link kinematics such as a stone or a box on a belt. **Top Right**: We model collisions through a spring-mass impact model with contact inertia I_{coll} and contact stiffness c transmits contact force $f_{\text{coll}}(t)$. For the whole contact duration Δt an impulse of τ'_{coll} is transmitted. **Bottom**: General DEA structure where a Harmonic Drive couples the rotor and Wave Generator (WG), the spring system and Circular Spline (CS) as well as the link and Flexspline (FS).

Traditionally, high torque density in actuators with electric motors is achieved through high gear ratios. However, this comes at the cost of gearboxes being susceptible to damage by mechanical impacts. While the elastic elements in SEAs and DEAs decouple motor and load inertia and thereby provide protection against high impact torques as demonstrated by [20]–[22], the elastic element in PEAs enables energy efficient cyclic motions [23], but does not provide robustness to impacts. Alternatively, mechanical robustness can be enhanced through mechanical clutches [24]–[28], which adds complexity and weight to the actuator, thereby reducing torque density.

In elastic actuators, the stiffness not only influences the

[1]The author is with the Robotic Systems Lab, ETH Zurich, 8092 Zurich, Switzerland.

[2] The authors are with the Institute of Robotics and Mechatronics, German Aerospace Center (DLR), 82234 Weßling, Germany, corresponding author: Anton Shu (anton.shu@dlr.de)

©2024 IEEE. Personal use of this material is permitted. Permission from IEEE must be obtained for all other uses, in any current or future media, including reprinting/republishing this material for advertising or promotional purposes, creating new collective works, for resale or redistribution to servers or lists, or reuse of any copyrighted component of this work in other works.

This article is published by IEEE with Digital Object Identifier (DOI):10.1109/TRO.2024.3422049

robustness to impacts, but also the open-loop torque bandwidth and thus the dynamic actuator performance. Increasing the stiffness in SEAs increases the resonance frequency and benefits torque tracking at the expense of actuator transparency [29] and robustness. However, it has no influence on the torque attenuation at frequencies above resonance which is characterized by 40dB/dec drop-offs for purely elastic SEAs and 20dB/dec for viscous-elastic ones. Implementing variable stiffness in all three categories of elastic actuators [30]–[42] and/or damping [43]–[45], allows adapting the open-loop torque bandwidth at the price of increased hardware complexity.

In contrast to SEAs and viscoelastic SEAs, Lauria et al. [9] and Lee et al. [46] found that DEAs better transmit high frequency torque components, since the open-loop transfer function from motor to joint torques has a plateau in the high frequency regime. This plateau is due to reaction forces of the spring-side inertia which can be influenced by the design engineer. Therefore, DEAs allow to enhance the open-loop torque bandwidth of the actuator and thus its performance. However, the higher this plateau is, the more susceptible the actuator becomes to mechanical impacts. Hence, a careful selection of the DEA parameters regarding application-specific robustness and performance is important. While there are some robustness and performance dependent stiffness selection rules for SEAs, there are insufficient design guidelines on how to balance robustness and open-loop torque bandwidth in DEAs. In this article, we aim at closing this gap by providing a design guide to balance the open-loop torque bandwidth and impact robustness in DEAs, which we consider as compact actuators for robotic applications that require high torque densities, high performance, and high robustness to impacts. This design guide uses a decision tree and closed-form formulas, as it is common in the motor and gear selection process.

We validate our approach using an experimental DEA that is equipped with a strain gauge-based torque sensor at the gear output. As an additional feature, the springs of our testbed can be locked to render the DEA into a conventional torque-controlled, cobot-like actuator, allowing for a direct comparison of both types of actuators.

In summary, we provide guidance for designing DEAs based on the trade-off between impact robustness and open-loop torque bandwidth with the following contributions:

- Approximations of the impact-related gear torque based on an analytical solution of the differential equations as robustness measure with experimental verification
- Equations to approximate the open-loop torque bandwidth and the associated gain as well as the finite high frequency open-loop torque gain as a performance measure with experimental verification
- A design guide for selecting the mechanical parameters of the actuator that allows an application-specific, model-based trade-off of performance and robustness
- A reconfigurable DEA design for experimental verification of the trade-off of performance and robustness

The paper is structured as follows. First, Sec. II presents the actuator model and its parameters as well as the collision model. Then, Sec. III defines performance and robustness measures and analyzes the influence of the design parameters on these measures for both open-loop torque bandwidth and impact-related gear load. Next, Sec. IV shows how these measures can be used to select actuator parameters. In the following Sec. V, a DEA design is introduced that was used to obtain the experimental results presented in Sec. VI. There, open-loop torque bandwidth, interaction stiffness control and impact experiments are presented. Sec. VII summarizes the results. Finally, the Appendix in Sec. VIII presents additional non-abbreviated equations for completeness.

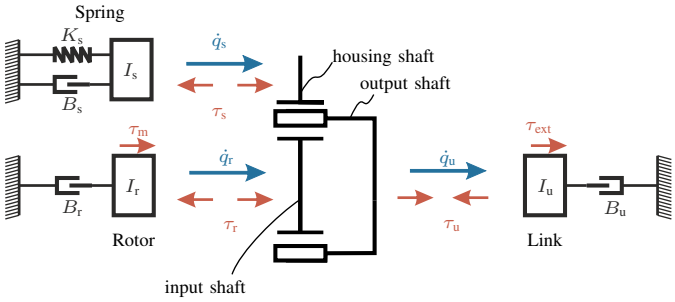

Fig. 2. Structure of a DEA. Rotor, link and spring are connected by a differential gearbox. Velocities are denoted with $\dot{q}_i$, torques with τ_i, inertia with I_i and damping values with B_i where $i \in \{\mathrm{r}, \mathrm{s}, \mathrm{u}\}$. Additional quantities are the stiffness K_s and the motor torque τ_m and the external torque τ_ext.

II. DEA and Collision

In this section we present the linear DEA model as well as the collision model.

A. Actuator Model

This section introduces a linear DEA model similar to [9], [46] as well as its parameters. These parameters can be influenced by the system designer to achieve a desired behavior. At the center of the actuator is a differential gear that couples three shafts with a kinematic constraint. As a result, the differential gear has two degrees of freedom. Members of this group are planetary gearboxes, cycloidal drives and harmonic drives. They are often used with one shaft fixed to the housing which results into a compact one degree of freedom transmission.

The inertia of the link I_u, the rotor I_r and the spring I_s are each connected to a different shaft of the differential gear. The spring-side inertia is supported against the housing with a spring of stiffness K_s. Additionally, each inertia is supported by a damper that models the bearing friction or deliberately introduced damping with the damping parameter B_r, B_s and B_u, respectively. The system is actuated by the electromagnetic motor torque τ_m which accelerates the rotor inertia. This rotor inertia is connected to the input shaft of the gearbox. Both rotate with the velocity $\dot{q}_\mathrm{r}$ and have an interfacing torque of τ_r. The spring is connected to the housing shaft of the gearbox. Both rotate with the velocity $\dot{q}_\mathrm{s}$ and have an interfacing torque of τ_s. Lastly, the link is connected to the output shaft of the gearbox, which both rotate with the velocity $\dot{q}_\mathrm{u}$ and have an interfacing torque of τ_u. The link exerts the torque τ_ext on the environment.

The structure, the nomenclature and the direction of velocities and torques are visualized in Fig. 2.

The Willis equation [47] describes the kinematic constraint that relates the velocities of shafts to the gear ratio $N < 0$ as $N = \frac{\dot{q}_\mathrm{r} - \dot{q}_\mathrm{s}}{\dot{q}_\mathrm{u} - \dot{q}_\mathrm{s}}$, which can be expressed as

$$\dot{q}_\mathrm{r} - N\dot{q}_\mathrm{u} + (N-1)\dot{q}_\mathrm{s} = 0. \tag{1}$$

We consider the gearbox a power continuous element, which implies

$$\dot{q}_\mathrm{r}\tau_\mathrm{r} + \dot{q}_\mathrm{s}\tau_\mathrm{s} + \dot{q}_\mathrm{u}\tau_\mathrm{u} = 0. \tag{2}$$

Since the torque ratios on the gearbox are invariant to the velocities [47], we can derive the torque ratio from rotor-side torque τ_r to link-side torque τ_u by choosing a spring velocity of $\dot{q}_\mathrm{s} = 0$ with (1) and (2) as

$$\tau_\mathrm{r} = -\tfrac{1}{N}\tau_\mathrm{u}. \tag{3}$$

With the torque equilibrium $\tau_\mathrm{r} + \tau_\mathrm{s} + \tau_\mathrm{u} = 0$, and (3) we can express the torques at the gearbox in respect to τ_s as $\tau_\mathrm{r} = \frac{1}{N-1}\tau_\mathrm{s}$ and $\tau_\mathrm{u} = -\frac{N}{N-1}\tau_\mathrm{s}$. Therefore, the dynamics of the system follows,

$$\begin{aligned} I_\mathrm{r}\ddot{q}_\mathrm{r} + B_\mathrm{r}\dot{q}_\mathrm{r} &= \tau_\mathrm{m} - \tau_\mathrm{r} = \tau_\mathrm{m} - \tfrac{1}{N-1}\tau_\mathrm{s}, \\ I_\mathrm{s}\ddot{q}_\mathrm{s} + B_\mathrm{s}\dot{q}_\mathrm{s} + K_\mathrm{s}q_\mathrm{s} &= -\tau_\mathrm{s}, \\ I_\mathrm{u}\ddot{q}_\mathrm{u} + B_\mathrm{u}\dot{q}_\mathrm{u} &= \tau_\mathrm{ext} - \tau_\mathrm{u} = \tau_\mathrm{ext} + \tfrac{N}{N-1}\tau_\mathrm{s}. \end{aligned} \tag{4}$$

For the following parameters, the model (4) is dynamically equivalent to that of a SEA with an additional damper: $I_{\mathrm{s,SEA}} = 0$, $B_{\mathrm{s,SEA}} = (N/(N-1))^2 B_\mathrm{s}$ and $K_{\mathrm{s,SEA}} = (N/(N-1))^2 K_\mathrm{s}$.

To transfer this model to the frequency domain we define transfer functions for rotor dynamics $P_\mathrm{r}(s) = (I_\mathrm{r}s^2 + B_\mathrm{r}s)^{-1}$, spring dynamics $P_\mathrm{s}(s) = (I_\mathrm{s}s^2 + B_\mathrm{s}s + K_\mathrm{s})^{-1}$ and link dynamics $P_\mathrm{u}(s) = (I_\mathrm{u}s^2 + B_\mathrm{u}s)^{-1}$ with the help (4).

The mapping from τ_m to τ_u in the frequency domain is denoted as Transmissibility $T(s) = \tau_\mathrm{u}/\tau_\mathrm{m}$ as,

$$T(s) = \frac{\tau_\mathrm{u}}{\tau_\mathrm{m}} = \frac{NP_\mathrm{r}(s)}{P_\mathrm{r}(s) + N^2P_\mathrm{u}(s) + (N-1)^2P_\mathrm{s}(s)}, \tag{5}$$

where a more detailed derivation is presented in Sec. VIII-A.

We want to highlight that the simple second order model we have chosen for the linear analysis of the following sections implies strong assumptions. Firstly, couplings to other joints are neglected. As such I_u is treated as a constant and analysis of extreme values as the minimum value ${I_\mathrm{u}}^-$ and maximum value ${I_\mathrm{u}}^+$ do not cover its time dependency. Secondly, a detailed actuator model is omitted. As such many additional effects that can greatly influence the actuator dynamic, like Coulomb friction, inter-gearbox dynamics (e.g. torque ripple) or nonlinear elasticities are not covered, but can be handled with proper control using disturbance observers [48]

B. Collision Model

This section introduces our collision model. We consider a collision that generates a collision torque $\tau_{\mathrm{ext,coll}}(t)$ on I_u and that transmits an impulse or torque shock τ'_coll for a contact duration of Δt. We assume a half-sine force profile illustrated on the top right of Fig. 1. This choice is motivated from a spring-mass collision model with impact inertia I_coll, contact stiffness c and pre-collision velocity Δv. For this model Δt and $\left|\tau'_\mathrm{coll}\right|$ can be calculated as

$$\Delta t = \pi\sqrt{I_\mathrm{coll}/c}, \tag{6}$$

$$\left|\tau'_\mathrm{coll}\right| = 2\Delta v I_\mathrm{coll}. \tag{7}$$

The maximum force occurs at $\Delta t/2$ and evaluates to

$$\tau_{\mathrm{ext,coll,max}} = \frac{\pi\tau'_\mathrm{coll}}{2\Delta t}. \tag{8}$$

In comparison to more detailed contact models where dissipation is considered [49]–[51] the spring-mass model transfers a maximum τ'_coll. Sec. VIII-A shows how the spring-mass model can be applied for a multi-link system to obtain both τ'_coll and Δt.

III. Performance and Robustness Measures

This section introduces our definitions of torque bandwidth and impact robustness for a DEA. These are quantified by the mechanical parameters I_i, B_i, K_s and N where $i \in \{\mathrm{r,s,u}\}$. These expressions are used for the design guideline in Sec. IV.

To define the torque bandwidth and impact robustness we use a performance and robustness measure in the frequency domain. As performance measure we use $T(s)$, since it is well established [9][46].

As robustness measure we are interested in an expression that relates τ_ext to a gearbox torque $\tau_i, i \in \{\mathrm{r,s,u}\}$. Since gearbox data sheets often reference τ_u [52] we define the Robustness $R(s) = \tau_\mathrm{u}/\tau_\mathrm{ext}$ as,

$$R(s) = \frac{\tau_\mathrm{u}}{\tau_\mathrm{ext}} = \frac{N^2P_\mathrm{u}(s)}{P_\mathrm{r}(s) + N^2P_\mathrm{u}(s) + (N-1)^2P_\mathrm{s}(s)}. \tag{9}$$

An alternative measure would be the output impedance $Z(s) = \tau_\mathrm{u}/\dot{q}_u$ of the actuator in combination with a velocity change $\Delta\dot{q}_\mathrm{u}$. Main difference between $R(s)$ and $Z(s)$ is that $Z(s)$ is not influenced by I_u and thus is a load inertia independent measure. However, in our view I_u is a parameter that is related to a functional component in the robot design process and the designer needs to account for its influence on the impact torque at the gears. Therefore, we are using the load inertia dependent $R(s)$ as robustness measure.

The rigid actuator is used as a comparative system. The respective Transmissibility $T_\mathrm{stiff}(s)$ and Robustness $R_\mathrm{stiff}(s)$ are obtained by fixing the housing shaft of the gear. For $T_\mathrm{stiff}(s)$ we describe this with

$$\begin{aligned} T_\mathrm{stiff}(s) &= \lim_{I_\mathrm{s}\to\infty} T(s) = \lim_{K_\mathrm{s}\to\infty} T(s) = \lim_{B_\mathrm{s}\to\infty} T(s) \\ &= \frac{-NI_\mathrm{u}s - NB_\mathrm{u}}{(N^2I_\mathrm{r} + I_\mathrm{u}s) + B_\mathrm{r} + B_\mathrm{u}}, \end{aligned} \tag{10}$$

and for $R_\mathrm{stiff}(s)$ similarly with

$$\begin{aligned} R_\mathrm{stiff}(s) &= \lim_{I_\mathrm{s}\to\infty} R(s) = \lim_{K_\mathrm{s}\to\infty} R(s) = \lim_{B_\mathrm{s}\to\infty} R(s) \\ &= \frac{N^2I_\mathrm{r}s + N^2B_\mathrm{r}}{(N^2I_\mathrm{r} + I_\mathrm{u})s + N^2B_\mathrm{r} + B_\mathrm{u}}. \end{aligned} \tag{11}$$

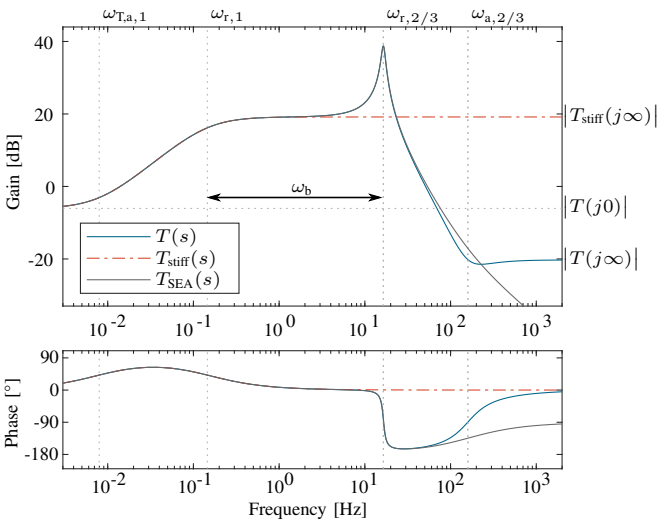

Fig. 3. Bode plot of the Transmissibility $T(s) = \tau_\mathrm{u}/\tau_\mathrm{m}$ for the $\underline{\mathrm{dea}}_\mathrm{hb}$ configuration. The torque bandwidth ω_b as well as the gains $|T(0)|$, $\lim_{\omega\to\infty}|T_{\mathrm{stiff}}(j\omega)|$, $\lim_{\omega\to\infty}|T(j\omega)|$ and corner frequencies $\omega_{\mathrm{a},1}$, $\omega_{\mathrm{r},1}$, $\omega_{\mathrm{a},2/3}$ and $\omega_{\mathrm{r},2/3}$ are highlighted. Parameters for the $\underline{\mathrm{dea}}_\mathrm{hb}$ configuration are given in Table III.

A. Open-Loop Torque Bandwidth

The following subsection analyzes the frequency response of $T(s)$ and $R(s)$. Based on an exemplary frequency response we define corner frequencies and stationary gains as well as the torque bandwidth for the scope of this publication. We then discuss the influence of $I_\mathrm{s}, B_\mathrm{s}$ and K_s on this torque bandwidth. With the help of two simplifications we compute closed-form equations on both gains and corner frequencies. Finally, we compare $T(s)$ and $R(s)$ in different frequency regions.

1) Definitions: Fig. 3 shows a Bode plot of $T(s)$ to give an intuitive understanding of the corner frequencies and stationary gains. To do so we have defined the exemplary high bandwidth DEA configuration $\underline{\mathrm{dea}}_\mathrm{hb}$. It serves as a baseline for a DEA design. Its parameters are listed in Table III.

From Fig. 3 we identify the resonance frequencies $\omega_{\mathrm{r},i}$, as well as the anti-resonance frequencies $\omega_{\mathrm{a},i}$ which are the corner frequencies of the system, where $\omega_{j,2} \leq \omega_{j,3}$ with $j \in \{\mathrm{a},\mathrm{r}\}$. We further identify the low frequency gains $|T(j0)|$ and $|R(j0)|$ as well as the high frequency gains for the elastic system $\lim_{\omega\to\infty}|T(j\omega)|$ and $\lim_{\omega\to\infty}|R(j\omega)|$ as well as the high frequency gains for the stiff system, respectively.

We define the open-loop torque bandwidth of the DEA ω_b on $T(s)$ as the frequency range between below that second resonant frequency $\omega_{\mathrm{r},2}$ and above of both of the first anti-resonance frequency $\omega_{\mathrm{T,a},1}$ of $T(s)$ and the first resonant frequency $\omega_{\mathrm{r},1}$

$$\{\omega_\mathrm{b} \,|\, \omega_\mathrm{b} \in [\max(\omega_{\mathrm{r},1}, \omega_{\mathrm{T,a},1}), \omega_{\mathrm{r},2}]\}. \tag{12}$$

We need to include $\omega_{\mathrm{T,a},1}$ in this definition since in theory it can become greater than $\omega_{\mathrm{r},1}$ as apparent from the values in Table II which is introduced in Sec. III-A4.

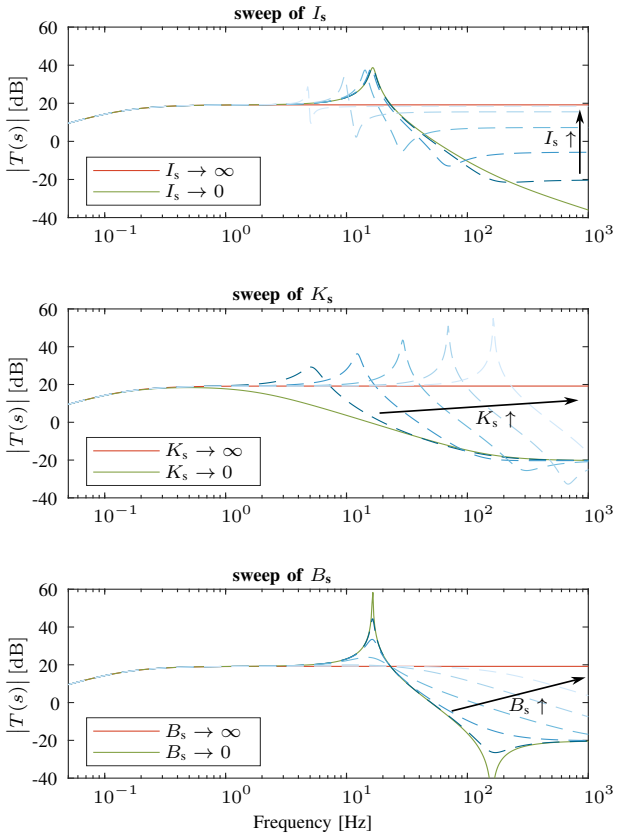

Fig. 4. Gain of the Transmissibility $|T(j\omega)|$ for different spring-side parameters. From Top to Bottom; I_s, K_s and B_s are varied in $[0,\infty)$ with all other parameters from the $\underline{\mathrm{dea}}_\mathrm{hb}$ configuration from Table III.

2) Influence of the Spring System: To illustrate the influence of the spring-side parameters I_s, K_s and B_s on $|T(j\omega)|$ and hence ω_b we vary these parameters individually for the $\underline{\mathrm{dea}}_\mathrm{hb}$ configuration in $[0,\infty)$. Fig. 4 shows the resulting gain over frequency plots.

For each $I_\mathrm{s} \to \infty$, $K_\mathrm{s} \to \infty$ and $B_\mathrm{s} \to \infty$ the actuator becomes stiff which is visualized in red. For $I_\mathrm{s} \to 0$ the actuator is transformed to a SEA with no finite high frequency gain as stated in Sec. II-A For rising values of I_s we observe a rising high frequency gain $\lim_{\omega\to\infty}|T(j\omega)|$ and smaller $\omega_{\mathrm{a},2/3}$ and $\omega_{\mathrm{r},2/3}$. From our experience the former effect dominates for practically relevant values of I_s. Rising values of K_s result in higher $\omega_{\mathrm{a},2/3}$ and $\omega_{\mathrm{r},2/3}$, greater $\left|T(j\omega_{\mathrm{r},2/3})\right|$ and smaller $\left|T(j\omega_{\mathrm{a},2/3})\right|$. In contrast, rising values of B_s result in higher $\omega_{\mathrm{a},2/3}$ and $\omega_{\mathrm{r},2/3}$ as well, however, the gain at these frequencies stands out less. In summary, a high stiffness K_s and a high spring-side inertia I_s and a high damping value B_s are beneficial for the performance of the actuator.

3) Simplifications: For some computations we need to simplify the introduced transfer functions. A first simplification known from literature [9][46] is to neglect damping. For $T(s)$ and $R(s)$ this results to

$$\hat{T}(s) = T(s)\Big|_{B_i=0}, i \in \{\mathrm{r},\mathrm{s},\mathrm{u}\} \tag{13}$$

$$\hat{R}(s) = R(s)\Big|_{B_i=0}, \tag{14}$$

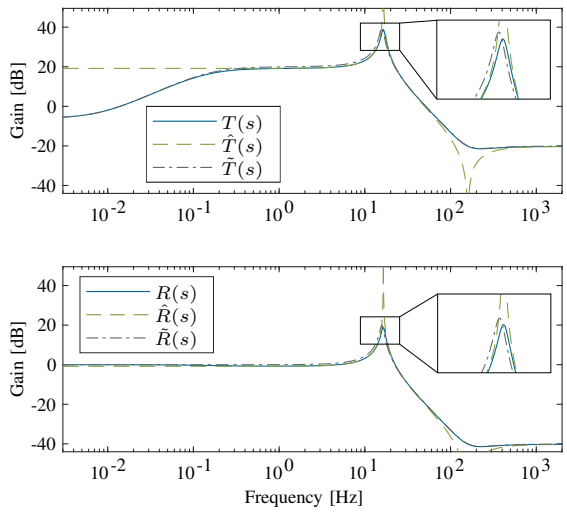

Fig. 5. Gain over frequency of Transmissibility $T(s) = \tau_{\mathrm{u}}/\tau_{\mathrm{m}}$ and Robustness $R(s) = \tau_{\mathrm{u}}/\tau_{\mathrm{ext}}$ together with approximations for the $\underline{\mathrm{dea}}_{\mathrm{hb}}$ configuration. Parameters for the $\underline{\mathrm{dea}}_{\mathrm{hb}}$ configuration are given in Table III.

with the shared denominator $D(s)$

$$\hat{D}(s) = D(s)\Big|_{B_i=0}, i \in \{\mathrm{r}, \mathrm{s}, \mathrm{u}\}. \tag{15}$$

However, the assumption of no damping is not valid for all DEAs. For example, in [45] damping is deliberately introduced. We therefore introduce a second simplification where we neglect all terms without the squared gear ratio N^2 in the denominator $D(s)$ as many robotic actuator designs use differential gearboxes with very high gear ratios and the gear ratio occurs squared in the denominator $D(s)$. The simplified denominator $\tilde{D}(s)$ is computed as,

$$\tilde{D}(s) = N^2 \lim_{N\to\infty} \frac{D(s)}{N^2}. \tag{16}$$

This results in the simplified transfer functions $\tilde{T}(s) = \mathrm{Num}(T(s))/\tilde{D}(s)$ and $\tilde{R}(s) = \mathrm{Num}(R(s))/\tilde{D}(s)$ where "Num" is an abbreviation for numerator. Fig. 5 visualizes both approximations on both $T(s)$ and $R(s)$. We present which terms are neglected in detail in Sec. VIII-B

4) Corner Frequencies and Stationary Gains: In the next step, we compute closed-form equations for the corner frequencies and stationary gains. Table I gives the limits for low frequencies $\omega \to 0$ and high frequencies $\omega \to \infty$ for all transfer functions. Since all entries of Table I are real-valued, the corresponding phase angles are zero.

Regarding the corner frequencies we compute antiresonance frequencies $\omega_{\mathrm{a},i}$ corresponding to roots of the respective numerator z_i, and antiresonance frequencies $\omega_{\mathrm{r},i}$ corresponding to the roots of the common denominator p_i. For a shorter variant of the expressions for $\omega_{\mathrm{r},i}$ we use the two simplifications (15) and (16) and arrive at expressions on the approximated resonance frequencies: For the assumption of no damping $\hat{\omega}_{\mathrm{r},i}$ associated to $\hat{D}(s)$ and for the assumption of a high gear ratio $\tilde{\omega}_{\mathrm{r},i}$ associated to $\tilde{D}(s)$. The expressions are listed in Table II together with the anti-resonance frequencies $\omega_{\mathrm{a},i}$. Sec. VI discusses the applicability of the used simplifications.

TABLE I
LOW AND HIGH FREQUENCY GAIN

	$\omega \to 0$		$\omega \to \infty$	
$T(j\omega)$	$\frac{-NB_{\mathrm{u}}}{B_{\mathrm{r}}N^2+B_{\mathrm{u}}}$	(19)	$\frac{-NI_{\mathrm{u}}I_{\mathrm{s}}}{((N-1)^2I_{\mathrm{r}}+I_{\mathrm{s}})I_{\mathrm{u}}+I_{\mathrm{r}}I_{\mathrm{s}}N^2}$	(20)
$\hat{T}(j\omega)$	$\frac{-NI_{\mathrm{u}}}{I_{\mathrm{r}}N^2+I_{\mathrm{u}}}$	(21)	$\frac{-NI_{\mathrm{s}}I_{\mathrm{u}}}{((-1+N)^2I_{\mathrm{r}}+I_{\mathrm{s}})I_{\mathrm{u}}+I_{\mathrm{r}}N^2I_{\mathrm{s}}}$	(22)
$\tilde{T}(j\omega)$	$\frac{-B_{\mathrm{u}}}{NB_{\mathrm{r}}}$	(23)	$\frac{-I_{\mathrm{s}}I_{\mathrm{u}}}{(I_{\mathrm{u}}+I_{\mathrm{s}})NI_{\mathrm{r}}}$	(24)
$T_{\mathrm{stiff}}(j\omega)$	$\frac{-NB_{\mathrm{u}}}{B_{\mathrm{r}}N^2+B_{\mathrm{u}}}$	(25)	$\frac{-NI_{\mathrm{u}}}{I_{\mathrm{r}}N^2+I_{\mathrm{u}}}$	(26)
$R(j\omega)$	$\frac{B_{\mathrm{r}}N^2}{B_{\mathrm{r}}N^2+B_{\mathrm{u}}}$	(27)	$\frac{N^2I_{\mathrm{r}}I_{\mathrm{s}}}{((N-1)^2I_{\mathrm{r}}+I_{\mathrm{s}})I_{\mathrm{u}}+I_{\mathrm{r}}I_{\mathrm{s}}N^2}$	(28)
$R_{\mathrm{stiff}}(j\omega)$	$\frac{B_{\mathrm{r}}N^2}{B_{\mathrm{r}}N^2+B_{\mathrm{u}}}$	(29)	$\frac{I_{\mathrm{r}}N^2}{I_{\mathrm{r}}N^2+I_{\mathrm{u}}}$	(30)

Analysis of the obtained results yields that both the $T(s)$ and $R(s)$ have one real pole-zero pair z_1, p_1, and two conjugate associate zeros and poles $z_2 = \overline{z}_3$, $p_2 = \overline{p}_3$. With $\tilde{\omega}_{\mathrm{r},1} = \omega_{\mathrm{a},1}$ for $\tilde{R}(s)$ the first pole and zero cancel. This is not the case for $R(s)$. Another interesting observation is, that with the assumption of no damping $\hat{\omega}_{\mathrm{r},1} = 0$, while $\tilde{\omega}_{\mathrm{r},1} \neq 0$. Thus, the assumption of a high gear ratio amplifies the rotor dynamics considerably, compared to the assumption of no damping.

5) Transmissibility and Robustness Trade-off: Knowledge of the corner frequencies and stationary gains allows comparing $T(s)$ and $R(s)$ in the frequency domain.

The summary in Table II shows, that in case of relevant frequencies the two transfer functions $T(s)$ and $R(s)$ only differ in their first anti-resonance frequency $\omega_{\mathrm{a},1}$. They cannot differ in the resonance frequencies $\omega_{\mathrm{r},i}$ since both functions share the same denominator.

Another way to distinguish both transfer characteristics is by their constant gains. From Table I we can conclude that their fraction in the low frequency region scales with

$$\frac{\left|R(j0)\right|}{\left|T(j0)\right|} = \frac{B_{\mathrm{r}}|N|}{B_{\mathrm{u}}}, \tag{17}$$

while in the high frequency region it scales with

$$\lim_{\omega\to\infty} \frac{\left|R(j\omega)\right|}{\left|T(j\omega)\right|} = \frac{I_{\mathrm{r}}|N|}{I_{\mathrm{u}}}. \tag{18}$$

In the medium frequency range above $\omega_{\mathrm{r},1}$ and $\omega_{\mathrm{a},1}$ but below $\omega_{\mathrm{r},2/3}$ and $\omega_{\mathrm{a},2/3}$ the gain of the Transmissibility $\left|T(j\omega)\right|$ approaches the high frequency gain of the stiff system $\lim_{\omega\to\infty}\left|T_{\mathrm{stiff}}(j\omega)\right|$, as visualized in Fig. 3. This is consistent to our definition of ω_{b} and allows us to state

$$\left|T(j\omega_{\mathrm{b}})\right| \approx \lim_{\omega\to\infty}\left|T_{\mathrm{stiff}}(j\omega)\right|. \tag{31}$$

In this frequency region, as well as above for frequencies where $\left|T(j\omega)\right| \approx \lim_{\omega\to\infty}\left|T(j\omega)\right|$ the phase $\angle(T(j\omega)) \approx 0$ which simplifies control on the respective frequencies.

TABLE II
CORNER FREQUENCIES

	$T(s)$	$R(s)$
$\omega_{\mathrm{a},1}$	$\omega_{\mathrm{T,a},1} = \frac{B_\mathrm{u}}{I_\mathrm{u}}$ (33)	$\omega_{\mathrm{R,a},1} = \frac{B_\mathrm{r}}{I_\mathrm{r}}$ (34)
$\omega_{\mathrm{a},2/3}$	$\left\lvert \frac{B_\mathrm{s} \pm \sqrt{B_\mathrm{s}^2 - 4 I_\mathrm{s} K_\mathrm{s})}}{2 I_\mathrm{s}} \right\rvert$ (35)	
$\hat{\omega}_{\mathrm{r},1}$	0 (36)	
$\hat{\omega}_{\mathrm{r},2/3}$	$\sqrt{\frac{K_\mathrm{s}(I_\mathrm{r} N^2 + I_\mathrm{u})}{((N-1)^2 I_\mathrm{r} + I_\mathrm{s}) I_\mathrm{u} + I_\mathrm{r} I_\mathrm{s} N^2}}$ (37)	
$\tilde{\omega}_{\mathrm{r},1}$	$\frac{B_\mathrm{r}}{I_\mathrm{r}}$ (38)	
$\tilde{\omega}_{\mathrm{rr},2/3}$	$\left\lvert \frac{B_\mathrm{u} + B_\mathrm{s} \pm \sqrt{(B_\mathrm{u} + B_\mathrm{s})^2 - 4(I_\mathrm{u} + I_\mathrm{s}) K_\mathrm{s}}}{2(I_\mathrm{u} + I_\mathrm{s})} \right\rvert$ (39)	

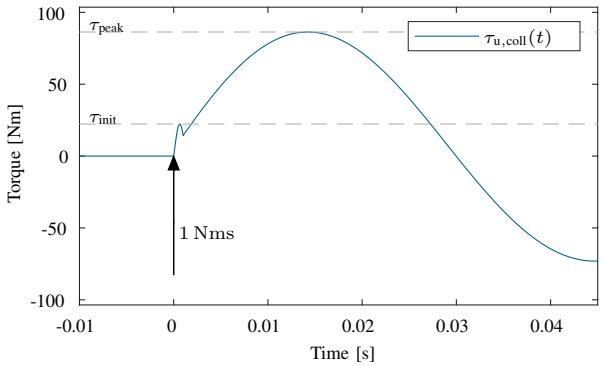

Fig. 6. Torque shock response $\tau_{\mathrm{u,coll}}(t)$ simulated with MATLAB *impulse* command. The impact is modeled as torque shock. The link-side torque instantly rises to a level of τ_{init} and proceeds to rise to τ_{peak} in a sine-like fashion. For this figure the $\underline{\mathrm{dea}}_{\mathrm{hb}}$ configuration from Table III is used.

Similarly to $\left|T(j\omega)\right|$, the gain of the Robustness $\left|R(j\omega)\right|$ approaches $\lim_{\omega\to\infty}\left|R_{\mathrm{stiff}}(j\omega)\right|$ for ω_b. This allows us to compare the fraction $T(j\omega_\mathrm{b})/R(j\omega_\mathrm{b})$ with

$$\frac{\left|R(j\omega_\mathrm{b})\right|}{\left|T(j\omega_\mathrm{b})\right|} \approx \lim_{\omega\to\infty} \frac{\left|R_{\mathrm{stiff}}(j\omega)\right|}{\left|T_{\mathrm{stiff}}(j\omega)\right|} = \frac{I_\mathrm{r}|N|}{I_\mathrm{u}}. \tag{32}$$

Interestingly in the frequency domain the spring-side system does not influence the fractions (17), (18) and (32).

Thus, the frequency domain analysis allows to dimension the Transmissibility $T(s)$ to a required bandwidth which is discussed in Sec. IV. However, the Robustness $R(s)$ amplifies similar frequencies. To analyze whether a DEA is robust enough, a different perspective of the problem is needed.

B. Impact-Related Gear Torque

In this section we derive worst-case approximations for peak values of link-side collision torque $\tau_{\mathrm{u,coll}}(t)$ which are important values in the selection of the actuator gearbox. An approximation for both its initial value τ_{init} and later peak value τ_{peak} is presented based on the transmitted joint-space impulse τ'_{coll} and collision duration Δt. First we present an analytical solution for $\tau_{\mathrm{u,coll}}(t)$ which we visualize by example. Then we derive the peak values with the help of simplifying assumptions.

With (82) given in the Appendix, (9), and the Laplace transform $\mathcal{L}$ we find for $\tau_{\mathrm{u,coll}}$ in time domain,

$$\tau_{\mathrm{u,coll}}(t) = \mathcal{L}^{-1}\{R(s)\mathcal{L}\{\tau_{\mathrm{ext,coll}}(t)\}(s)\}(t). \tag{40}$$

A simulation of (40) is visualized in Fig. 6. This figure shows that the torque increases to an initial value at the time of impact as $\tau_{\mathrm{u,coll}}(t \approx 0) = \tau_{\mathrm{init}}$. After this initial rise a sine-like oscillation follows that reaches its first and highest maximum of τ_{peak}.

Closer inspection of (40) using the symbolic math software MAPLE 2023 shows that $\tau_{\mathrm{u,coll}}(t)$ is a sum of the scaled collision force $X(t)$ and the dynamic collision response $Y(t)$

$$\begin{aligned}\tau_{\mathrm{u,coll}}(t) = &\underbrace{a\mathcal{L}^{-1}\{\tau_{\mathrm{ext,coll}}(s)\}(t)}_{X(t)} \\ &+ \underbrace{b(t) * \mathcal{L}^{-1}\{\tau_{\mathrm{ext,coll}}(s)\}(t)}_{Y(t)},\end{aligned} \tag{41}$$

where the constant factor a results to

$$a = \frac{N^2 I_\mathrm{r} I_\mathrm{s}}{(N-1)^2 I_\mathrm{r} I_\mathrm{u} + N^2 I_\mathrm{r} I_\mathrm{s} + I_\mathrm{s} I_\mathrm{u}}, \tag{42}$$

and $b(t)$ is a too long expression to be presented.

To simplify (41) we first separate $X(t)$ and $Y(t)$ in their respective time domain with the assumption that the contact duration is much faster than the post-impact dynamics $\Delta t/\pi << \omega_{\mathrm{r},2/3}$

$$\tau_{\mathrm{u,coll}}(t) \approx \begin{cases} X(t) + Y(0) & t \in [0, \Delta t], \\ Y(t) & t > \Delta t, \end{cases} \tag{43}$$

To evaluate $Y(t)$ we use the Dirac-delta function $\delta(t)$ for an approximation of $\tau_{\mathrm{ext,coll}}(t)$ where the same impulse is transmitted, but infinite torque is implied similar to (75) given in the Appendix

$$\tau_{\mathrm{ext,coll}}(t) \approx \tau'_{\mathrm{coll}}\delta(t), \tag{44}$$

$$Y(t) \approx b(t)\tau'_{\mathrm{coll}}. \tag{45}$$

With $\tau_{\mathrm{ext,coll}}(\Delta t/2) = \tau_{\mathrm{ext,coll,max}}$ we then approximate τ_{init} with (8)

$$\tau_{\mathrm{init}} \approx X(\tfrac{\Delta t}{2}) + Y(0) \approx (a\tfrac{\pi}{2\Delta t} + b(0))\tau'_{\mathrm{ext,coll}}, \tag{46}$$

where $b(0)$ evaluates to

$$b(0) = \frac{N^2(N-1)^2 I_\mathrm{r}^2 (B_\mathrm{s} I_\mathrm{u} - B_\mathrm{u} I_\mathrm{s}) + N^2 I_\mathrm{s}^2 (B_\mathrm{r} I_\mathrm{u} - B_\mathrm{u} I_\mathrm{r})}{((N-1)^2 I_\mathrm{r} I_\mathrm{u} + N^2 I_\mathrm{r} I_\mathrm{s} + I_\mathrm{u} I_\mathrm{s})^2}. \tag{47}$$

Both simplifications from Sec. III-A yield an approximation on τ_{peak}. With the assumption of no damping (14) we approximate $b(t)$ as $\hat{b}(t)$ and τ_{peak} as $\hat{\tau}_{\mathrm{peak}}$

$$\hat{b}(t) = \frac{\hat{\tau}_{\mathrm{peak}}}{\tau'_{\mathrm{coll}}} \sin(\hat{\omega}_{\mathrm{r},2/3} t), \tag{48}$$

$$\hat{\tau}_{\mathrm{peak}} = \frac{I_\mathrm{u} N^2 I_\mathrm{r}^2 (N-1)^2 \sqrt{K_\mathrm{s}}}{\sqrt{((N-1)^2 I_\mathrm{r} I_\mathrm{u} + I_\mathrm{s} I_\mathrm{u} + N^2 I_\mathrm{r} I_\mathrm{s})^3 (N^2 I_\mathrm{r} + I_\mathrm{u})}} \tau'_{\mathrm{coll}}. \tag{49}$$

Approximation on $\tilde{b}(t)$ and respective peak torque $\tilde{\tau}_{\mathrm{peak}}$ for the assumption of a high gear ratio (16) is presented in Sec. VIII-B

With the expressions on τ_{init} and both $\hat{\tau}_{\mathrm{peak}}$ and $\tilde{\tau}_{\mathrm{peak}}$ the actuator can be dimensioned with respect to expected torque shocks which is presented in the next section.

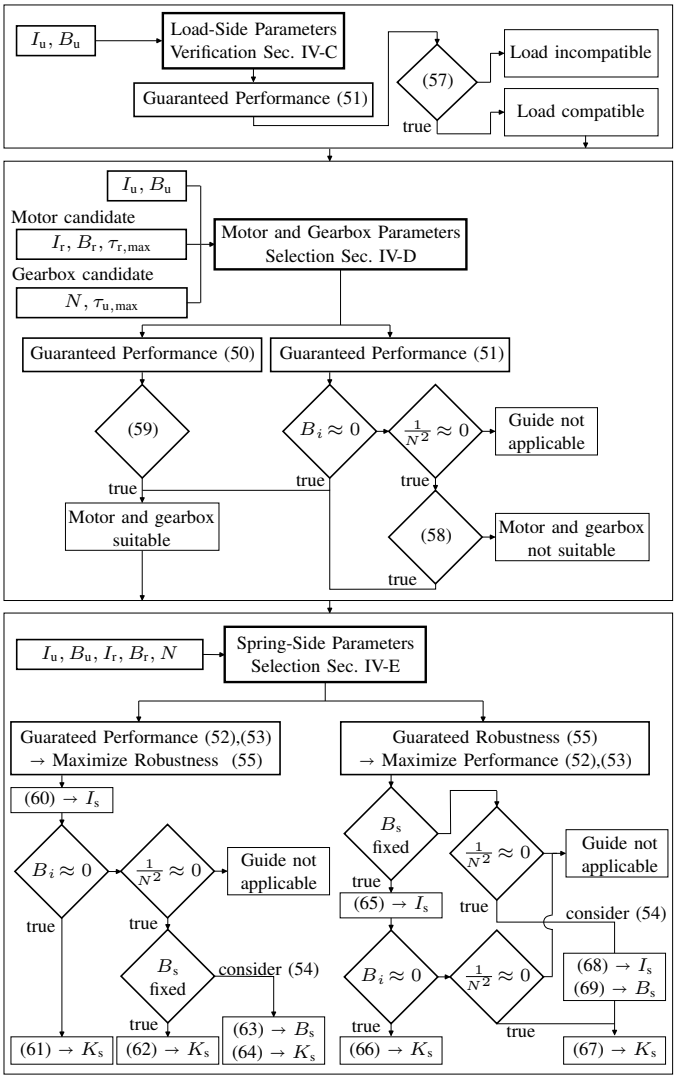

Fig. 7. Design guide process for a DEA. Each sub-process lists input parameters and applied design criteria defined in Sec. IV-A. The abbreviations $B_i \approx 0$ and $1/N^2 \approx 0$ denote simplifications defined in Sec. III-A3, with their applicability being discussed in Sec. IV-B. **Top**: Process to verify compatibility of the load with the performance requirement (51). **Middle**: Process to verify compatibility of the selected motor and gearbox. **Bottom**: Process to select the spring-side parameters. Two variants are presented, one to dimension the DEA in accordance to performance requirements whilst maximizing robustness and one to dimension the DEA in accordance to a robustness requirement whilst maximizing performance.

IV. Design Guide

This section shows how the mechanical parameters of a DEA can be selected to trade off open-loop torque bandwidth and robustness against impacts. First, criteria for performance and robustness are defined. Then, the motor and gearbox selection is discussed followed by a discussion of the applicability of the introduced simplifications. Finally, a procedure is introduced on the selection of K_s, I_s and B_s. For this guideline we assume that the link-side parameters of $I_\mathrm{u} \in [I_\mathrm{u}^-, I_\mathrm{u}^+]$ and B_u are known since they are application-specific. Fig. 7 visualizes the process.

TABLE III
Exemplary DEA configurations.

	$\underline{\text{dea}}_{\text{hb}}$	$\underline{\text{dea}}_{\text{perf}}$	$\underline{\text{dea}}_{\text{perf,damp}}$	$\underline{\text{dea}}_{\text{rob}}$	$\underline{\text{dea}}_{\text{rob,damp}}$
$I_\mathrm{s}[\mathrm{kgm}^2]$	1.00e-2	6.11e-2	6.11e-2	4.14e-0	1.15e-2
$I_\mathrm{r}[\mathrm{kgm}^2]$	1.00e-3	1.00e-3	1.00e-3	1.00e-3	1.00e-3
$I_\mathrm{u}[\mathrm{kgm}^2]$	1.00e+0	1.00e+0	1.00e+0	1.00e+0	1.00e+0
$K_\mathrm{s}[\frac{\mathrm{N\,m}}{\mathrm{rad}}]$	1.00e+4	3.51e+4	3.77e+4	6.27e+3	5.71e+3
N	-100	-100	-100	-100	-100
$B_\mathrm{r}[\frac{\mathrm{N\,m\,s}}{\mathrm{rad}}]$	1.00e-3	1.00e-3	1.00e-3	1.00e-3	1.00e-3
$B_\mathrm{s}[\frac{\mathrm{N\,m\,s}}{\mathrm{rad}}]$	1.00e+1	1.00e+1	4.00e+2	1.00e+1	5.49e+1
$B_\mathrm{u}[\frac{\mathrm{N\,m\,s}}{\mathrm{rad}}]$	5.00e-2	5.00e-2	5.00e-2	5.00e-2	5.00e-2

A. Performance Criteria

Regarding the performance of the actuator, we define three criteria. First, we summarize the ability of the actuator to perform dynamic torque profiles within the torque bandwidth as open-loop torque bandwidth requirement. We define this as the ability of the actuator to replicate sinusoidal oscillations with link-side torque amplitude $\tau_{\mathrm{u,req}}$ on I_u^+ within the required bandwidth $\omega_{\mathrm{b,req}} \in [\omega_{\mathrm{b,req},1}, \omega_{\mathrm{b,req},2}]$ (see (12)). We summarize this requirement as open-loop torque bandwidth requirement

$$\left|T_{\mathrm{stiff}}(j\omega_{\mathrm{b,req}})\right| \Big|_{I_u^+} \tau_{\mathrm{m,max}} \geq \tau_{\mathrm{u,req}}, \tag{50}$$

$$\max(\omega_{T,\mathrm{a},1}, \omega_{\mathrm{r},1}) \leq \omega_{\mathrm{b,req},1}, \tag{51}$$

$$\omega_{\mathrm{r},2} \geq \omega_{\mathrm{b,req},2}. \tag{52}$$

Second, we aim for an actuator that can maintain a minimum torque at high frequencies by asking that gain of the Transmissibility Ψ is present with I_u^-

$$\Psi \leq \lim_{\omega\to\infty} \left|T_{\mathrm{req}}(j\omega)\right| \Big|_{I_u^-}. \tag{53}$$

Third, we ask that the excessive gain at the resonance frequency $\omega_{\mathrm{r},2/3}$ is minimized to ease control near $\omega_{\mathrm{r},2/3}$

$$\left(\frac{\left|T_{\mathrm{req}}(j\omega_{\mathrm{r},2/3})\right|}{\lim_{\omega\to\infty}\left|T_{\mathrm{stiff}}(j\omega_{\mathrm{r},2/3})\right|}\right) \approx 1. \tag{54}$$

Regarding the robustness of the actuator, we formulate that the actuator has to withstand impacts which transmit a joint-space impulse of $\tau'_{\mathrm{coll,req}}$ with a duration of Δt on I_u^-. This implies that the link side torque is always smaller than the smallest maximum torque of the used components $\tau_{\mathrm{u,max}}$ as

$$\left|\tau_{\mathrm{u,coll}}(t)\Big|_{\tau'_{\mathrm{coll,req}},\Delta t, I_u^-}\right| < \tau_{\mathrm{u,max}}. \tag{55}$$

To simplify the following equations, we define the normalized impact force $\Phi = \tau_{\mathrm{u,max}}/\left|\tau'_{\mathrm{coll}}\right|$ and the fraction of scaled collision force and initial dynamic collision response $\Xi = b(0)/(a\tau_{\mathrm{ext,coll,max}})$ from (47). Higher values of Ξ will in general result in a more damped system with smaller values of $\lim_{\omega\to\infty}\left|T(j\omega)\right|$.

B. Validation of Simplifications

Sec. III-A introduces two simplifications, one where damping is neglected (15) and one where a high gear ratio is assumed (16). From our experience the assumption of no damping is valid for systems without deliberately introduced damping. The assumption of a high gear ratio can in our experience be used for systems with $|N| > 100$ and not deliberately introduced link-side damping B_u. The applicability of the high gear ratio simplification can be tested with

$$\left|T(j0)\right| - \left|\tilde{T}(j0)\right| = \frac{B_\mathrm{u}^2}{N B_\mathrm{r}(N^2 B_\mathrm{r} + B_\mathrm{u})} \approx 0. \tag{56}$$

Sec. III-B has introduced the assumption that the contact duration is much faster than the post-impact dynamics $\Delta t/\pi << \omega_{\mathrm{r},2/3}$. From our experience both values should differ by one magnitude.

C. Load-Side Parameters Verification

The first step of the design process is to check if the bandwidth requirement (51) is compatible with the load-side parameters

$$\omega_{\mathrm{b,req},1} \geq \omega_{\mathrm{T,a},1} = \frac{B_\mathrm{u}}{I_\mathrm{u}}. \tag{57}$$

If this is not the case it is not guaranteed that $\angle(T(i\omega_{\mathrm{b,req}})) < 0$.

D. Motor and Gearbox Parameters Selection

The second step is to verify that the selected motor and gearbox are compatible with the criteria. Regarding the bandwidth requirement (51) we find that it follows from (36) that with the approximation of no damping (51) it is always valid. For the approximation of a high gear ratio we find with (38) from (51) that

$$\frac{B_\mathrm{r}}{I_\mathrm{r}} < \omega_{\mathrm{b,req},1}. \tag{58}$$

Regarding (50) we find with (26)

$$\tau_\mathrm{m} = \frac{N I_{\mathrm{u},}^+}{N^2 I_\mathrm{r} + I_\mathrm{u}^+} \tau_{\mathrm{u,req}}. \tag{59}$$

In summary (58) and (59) allow comparing different choices of motors with sets of $\{B_\mathrm{r}, I_\mathrm{r}, \tau_{\mathrm{m,max}}\}$ and gearboxes with sets of $\{N, \tau_{\mathrm{u,max}}\}$ regarding both (50) and (51). If several sets of motors and gearboxes satisfy (50) and (51), we can choose the option with the best trade-off for the robustness. Apart from choosing a combination with high $\tau_{\mathrm{u,max}}$ we can deduce from (17),(18) and (32) that a low gear ratio N, low rotor-side inertia I_r, low rotor-side damping B_r emphasize $\left|T(j\omega)\right|$ against $\left|R(j\omega)\right|$. This is similar to the findings of [53], [54].

E. Spring-Side Parameters Selection

Lastly, the spring-side system parameters I_s, K_s and B_s are chosen. We show two variants; the design of the least performant actuator still satisfies the performance requirements and maximizes its robustness in Sec. IV-E1 and the design of the least robust actuator that still satisfies the robustness requirement and maximizes performance in Sec. IV-E2.

1) Guaranteed Performance: In this subsection values for I_s, K_s and optionally B_s are selected to maximize robustness and to meet the performance criteria. After this process it should be tested if the robustness criterion (55) is satisfied with (46) and (49) or (93).

First, the required spring side inertia I_s for (53) can be computed with (20) as,

$$I_\mathrm{s} = \frac{-I_\mathrm{u}^- I_\mathrm{r}(N-1)^2 \Psi}{I_\mathrm{u}^- N + (I_\mathrm{r} N^2 + I_\mathrm{u}^-)\Psi}. \tag{60}$$

For $\Psi \approx 0$, the inertia I_s should be chosen as small as possible.

The required stiffness K_s follows with the assumption of no damping

$$K_\mathrm{s} = \frac{I_\mathrm{u}^+ I_\mathrm{r}(N-1)^2 + I_\mathrm{r} I_\mathrm{s} N^2 + I_\mathrm{u}^+ I_\mathrm{s}}{I_\mathrm{r} N^2 + I_\mathrm{u}^+} \omega_{\mathrm{b,req},2}^2, \tag{61}$$

and for the assumption of high gear ratio

$$K_\mathrm{s} = \frac{2(B_\mathrm{u} + B_\mathrm{s})^2 - 4(I_\mathrm{u}^+ + I_\mathrm{s})^2 \omega_{\mathrm{b,req},2}}{4(I_\mathrm{u}^+ + I_\mathrm{s})}. \tag{62}$$

In case B_s can be tuned, we ask that $\tilde{T}(s)$ is critically damped and choose I_s from (60). From (39) B_s and K_s follow

$$B_\mathrm{s} = 2\omega_{\mathrm{b,req},2}(I_\mathrm{u}^+ + I_\mathrm{s}) - B_\mathrm{u}, \tag{63}$$

$$K_\mathrm{s} = \frac{(B_\mathrm{u} + B_\mathrm{s})^2}{4(I_\mathrm{u}^+ + I_\mathrm{s})}. \tag{64}$$

As an example, we use (60)-(64) to redesign $\underline{\mathrm{dea}}_{\mathrm{hb}}$ to match $\Psi = -5\,\mathrm{dB}$ and $\omega_{\mathrm{b,req}} = 30\,\mathrm{Hz}$ for both fixed and tunable B_s. The resulting configurations $\underline{\mathrm{dea}}_{\mathrm{perf}}$ and $\underline{\mathrm{dea}}_{\mathrm{perf,damp}}$ are given in Table III and visualized with the frequency gain and impact response on the left of Fig. 8.

2) Guaranteed Robustness: In this subsection values for I_s, K_s and optionally B_s are selected to maximize performance while meeting robustness criteria. After this process it should be tested if performance criteria (52),(53) are satisfied with (20) and (37) or (39).

We use the normalized impact force Φ to compute I_s from τ_{init} with (47)

$$I_\mathrm{s} = \frac{(N-1) I_\mathrm{r}(\alpha_1 + \sqrt{\alpha_2 + \alpha_3 + \alpha_4})}{(2 I_\mathrm{r} N^2 + 2 I_\mathrm{u}^-)^2 \Phi \Delta t + 2N^2(2\Delta t(B_\mathrm{u} I_\mathrm{r} - B_\mathrm{r} I_\mathrm{u}^-) - I_\mathrm{r}\pi(I_\mathrm{r} N^2 + I_\mathrm{u}^-))}, \tag{65}$$

where

$$\begin{aligned}
\alpha_1 &= -4(N-1)\left(I_\mathrm{r}\left(\left(\Phi I_\mathrm{u}^- + \tfrac{B_\mathrm{u}}{2}\right)\Delta t - \tfrac{I_\mathrm{u}^- \pi}{4}\right) N^2 + \Delta t\, {I_\mathrm{u}^-}^2 \Phi\right), \\
\alpha_2 &= 16\left(B_\mathrm{s} + (N-1)^2 B_\mathrm{r}\right)\Delta t^2 \Phi\, {I_\mathrm{u}^-}^3 + 4N^2 {B_\mathrm{u}}^2 {I_\mathrm{r}}^2 \Delta t^2 (N-1)^2, \\
\alpha_3 &= N^2 {I_\mathrm{u}^-}^2\left(\pi^2 (N-1)^2 {I_\mathrm{r}}^2 - 8 B_\mathrm{s} \Delta t(-4\Phi\Delta t + \pi) I_\mathrm{r} - 16 B_\mathrm{r} B_\mathrm{s} \Delta t^2\right), \\
\alpha_4 &= -4 I_\mathrm{r} I_\mathrm{u}^- \Delta t N^2\left(\left((N-1)^2(-4\Phi\Delta t + \pi) I_\mathrm{r} - 4\Delta t B_\mathrm{s}\right) B_\mathrm{u}\right. \\
&\quad \left. + 2N^2 B_\mathrm{s} I_\mathrm{r}(-2\Phi\Delta t + \pi)\right).
\end{aligned}$$

For $\Psi \approx 0$ the inertia I_s should be chosen as small as possible.

With the assumption of no damping K_s, follows from (49)

$$K_\mathrm{s} = \frac{(((N-1)^2 I_\mathrm{r} + I_\mathrm{s}) I_\mathrm{u}^- + I_\mathrm{r} I_\mathrm{s} N^2)^3 (I_\mathrm{r} N^2 + I_\mathrm{u}^-)}{(N-1)^4 I_\mathrm{r}^4 N^4 (I_\mathrm{u}^-)^2} \Phi^2. \tag{66}$$

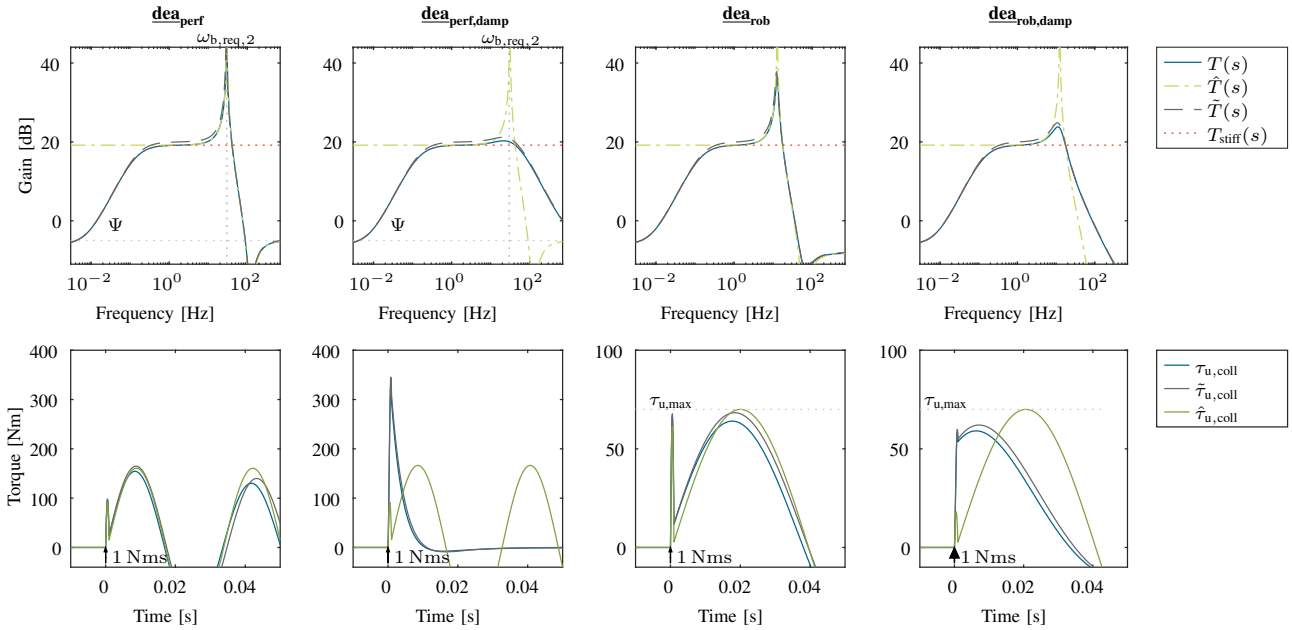

Fig. 8. Transmissibility and impact-related gear stress for different DEA configurations designed in Sec. IV-E1 and IV-E2. Different approximations are shown in green and gray. Parameters of the configurations are found in Table III.
dea$_{\text{perf}}$: dea$_{\text{hb}}$ is modified to show a high frequency gain $\Psi = -5\,\text{dB}$ and a required corner frequency $\omega_{\text{b,req},2} = 30\,\text{Hz}$. dea$_{\text{perf,damp}}$: additionally to dea$_{\text{perf}}$the resonance peak is minimized. dea$_{\text{rob}}$: dea$_{\text{hb}}$ is modified for a maximum impact-related gear torque $\tau_{\text{u,max}} = 70\,\text{Nm}$ dea$_{\text{rob,damp}}$: additionally to dea$_{\text{rob}}$the resonance peak is minimized.

For the assumption of a high gear ratio, K_s can be obtained by iteratively solving (93) with

$$K_\text{s} = \arg(\tau_{\text{u},max} = \tilde{\tau}_{peak}), \tag{67}$$

where from our experience (66) computes a good starting value. In case B_s can be tuned, we use Ξ and Φ given in Sec. IV-A to compute I_s and B_s

$$I_s = \frac{2\Delta t I_\text{u}^- I_\text{r} \Phi (N-1)^2}{(I_\text{r}(-2\Phi\Delta t + \pi(\Xi+1))N^2 - 2\Phi I_\text{u}^- \Delta t)}, \tag{68}$$

$$\begin{aligned} B_s = &\frac{N^2 I_\text{r}^2 \Phi (N-1)^2(-4B_\text{u}\Delta t^2\Phi + 2\pi B_\text{u}(\Xi+1)\Delta t)}{(I_\text{r}(-2\Phi\Delta t + \pi(\Xi+1))N^2 - 2\Phi I_\text{u}^- \Delta t)^2} \\ &+ \frac{N^2 I_\text{r}^2 \Phi (N-1)^2 \pi^2 I_\text{u}^- \Xi(\Xi+1)}{(I_\text{r}(-2\Phi\Delta t + \pi(\Xi+1))N^2 - 2\Phi I_\text{u}^- \Delta t)^2} \\ &- \frac{(4B_\text{r}\Delta t^2 (I_\text{u}^-)^2\Phi)\Phi(N-1)^2}{(I_\text{r}(-2\Phi\Delta t + \pi(\Xi+1))N^2 - 2\Phi I_\text{u}^- \Delta t)^2}. \end{aligned} \tag{69}$$

To find K_s (67) is used.

As an example, we use (65)-(68) to redesign dea$_{\text{hb}}$ to match $\tau_{\text{u,max}} = 70\,\text{Nm}$ with $\tau'_{\text{coll}} = 1\,\text{Nms}$ and without tunable B_s. In the latter case we use a value of $\Xi = 3$. The resulting configurations dea$_{\text{rob}}$ and dea$_{\text{rob,damp}}$ are given in Table III and visualized with the frequency gain and impact response on the right of Fig. 8.

F. Discussion

This section showed a possible approach to select DEA parameters when link-side parameters B_u and I_u are known. An important precondition is to evaluate which simplifications are applicable. The design guide proposes an alternative approach for each step when only one of the approximations is applicable. If none is applicable we recommend using the analytical solution of the differential equations directly.

TABLE IV
ACTUATOR REQUIREMENTS

Range of motion	300°
Maximum velocity	3 rad/s
Maximum torque	150 Nm
Spring stiffness range	50 - 500 Nm/rad
Spring deflection	55°
Maximum radial load	5 kN

V. Design of an Experimental DEA

We design a DEA as an experimental testbed that allows to test for impact robustness and torque bandwidth at different parameter settings. For the design we require, that the actuator can be reconfigured from a highly elastic configuration to a quasi-rigid configuration to allow further comparison with a standard torque-controlled actuator. We size the experimental DEA such that it could be used in the suspension of a larger mobile robot or as the base joint of a strong Cobot arm. To rule out error from up-scaling of an experimental design, we further require, that the DEA has sufficient joint torque and radial load capacity for full scale impact experiments. Table IV lists requirements for the actuator.

The resulting actuator design is shown in Fig. 9 and consists of three movable assemblies that are supported by separate bearings in the housing. They are connected via a Harmonic Drive CPL25 gearbox with a transmission ratio of $N = -160$, where the rotor drives the Wave Generator (WG), the link is connected to the Flexspline (FS) and the spring system is connected to the Circular Spline (CS).

A modified SARA [55] motor is used, which is based on the TQ ILM85x13 stator rotor combination. An absolute 18 bit

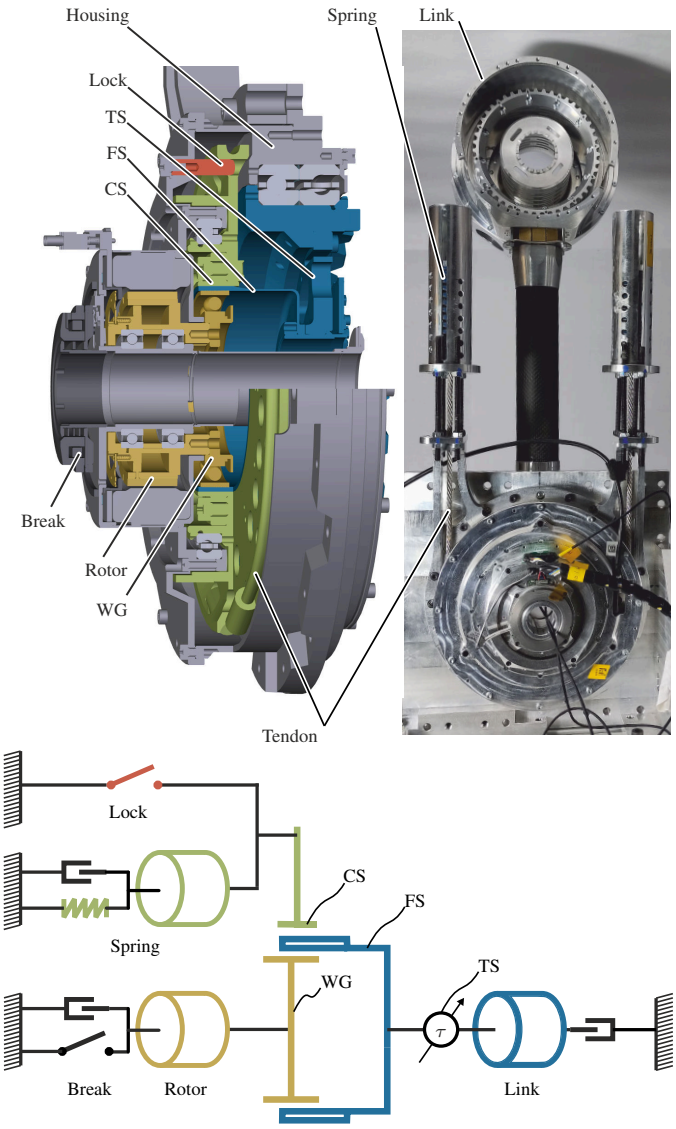

Fig. 9. DEA design that can be reconfigured to different highly elastic configurations and a quasi-rigid configuration for an application-specific, experimental trade-off between performance and robustness. A differential gear which is implemented as Harmonic Drive couples the rotor and Wave Generator (WG), the spring system and Circular Spline (CS) as well as the link and Flexspline (FS). The link-side torques are measured using a torque sensor (TS). Dowel pins (Lock) can be used to stop the spring system from moving, converting the actuator to a quasi-rigid actuator. A rotor-side brake can stop rotor movement. Left: Cutaway view of the actuator. Right: Photo with attached springs and link inertia. Bottom: Actuator structure.

iC-Haus MU-150 hall sensor measures the rotor position q_r. A SARA holding brake can lock the rotor position. The output is supported by KAYDON K140D bearings in O-configuration to support the radial load. The SARA torque sensor rated with $150\,\mathrm{Nm}$ is used to measure the output torque τ_u. An absolute $18\,\mathrm{bit}$ iC-Haus MU-150 sensor is used to measure the output position q_u against the hollow shaft housing. The spring system consists of two antagonist compression springs and a rotationally supported pulley which is connected to the CS. The springs are connected to the pulley with $4\,\mathrm{mm}$ Carlstahl tendons. The pulley has dedicated pockets to hold the tendon terminations. The compression spring housing is supported by threaded pins that allow to change the distance of springs and pulley and thus the pretension of the springs. Three dowel pins can be inserted to lock the rotational pulley in position, thus blocking the CS movement and reconfiguring the actuator into a quasi-rigid configuration. A $20\,\mathrm{bit}$ Bogen AKS17 sensor is used to measure the spring position q_s.

The design allows for a rotation of the CS of 114°. This is analogous of about $150\,\mathrm{mm}$ length change in each spring. Currently, off-the-shelf compression springs are used in this assembly. The modular nature of the design also allows mounting more complex systems than just springs. For example, additional weights can be attached to modify the spring-side inertia I_s.

The torque sensor allows to experimentally evaluate both torque bandwidth and impact robustness. It further can be used for control applications on the quasi-rigid configuration. Furthermore, both the springs can be switched, and the locking mechanism can be engaged while the actuator is both mounted to a link and ground. With all necessary sensors integrated, this enables to vary spring-side parameters to the extreme of a quasi-rigid configuration within an application scenario. This allows to experimentally tune the performance and robustness trade-off.

Since we have chosen a high gear ratio $|N| = 160$ and heavy-duty bearings with possibly high damping we expect that the assumption of a high gear ratio (16) will estimate the behavior of the actuator more accurately than the assumption of no damping (13).

VI. Experimental Evaluation

In this section, we experimentally evaluate the frequency response prediction, the controllability, and the impact torque predictions of the presented DEA as an example. Furthermore, we evaluate the presented simplifications.

For all experiments we are using a SARA [55] drive control unit to control the actuator. All measurements are recorded with $4\,\mathrm{kHz}$. The associated inverters are running in $40\,\mathrm{kHz}$ and allow $20\,\mathrm{A}$ current at $48\,\mathrm{V}$. The actuator is mounted on a test bench table and moves in the horizontal plane for all experiments. The τ_u signal is recorded with the internal torque sensor which is placed between the link and the gearbox as visualized in the bottom part of Fig. 9. Three different actuator configurations are evaluated. In the medium bandwidth configuration $\underline{\mathrm{dea}}_\mathrm{mb}$, I_s is as small as possible and K_s is designed with (66) where $\tau'_\mathrm{coll,req} = 4\,\mathrm{Nms}$. However, slightly weaker springs were used due to limited availability. The low bandwidth configuration $\underline{\mathrm{dea}}_\mathrm{lb}$ was designed to measure $\lim_{\omega\to\infty}\left|T(j\omega)\right|$ with a reduced value of K_s and an increased and I_s. However, the horizontal placement of the actuator limits the ability to modify I_s arbitrarily in our setup. Lastly, for the quasi-rigid $\underline{\mathrm{qr}}$ configuration the spring movement is locked. The dominating elastic element for the $\underline{\mathrm{qr}}$ configuration are thus the intrinsic stiffness and damping of the gearbox and the torque sensor which are in series with the gearbox and the joint. We thus set $I_{\mathrm{s},\underline{\mathrm{qr}}} = 0$ to match the series elastic behavior. The parameters of the used configurations are summarized in Table V where the inertia I_u,I_r and I_s

TABLE V
EXPERIMENTAL DEA CONFIGURATIONS. STARRED VALUES ARE ESTIMATES

	$\underline{\text{dea}}_{\text{mb}}$	$\underline{\text{dea}}_{\text{lb}}$	$\underline{\text{qr}}$
$I_{\text{s}}[\text{kgm}^2]$	1.90e-3	4.71e-3	0
$I_{\text{r}}[\text{kgm}^2]$	1.40e-4	1.40e-4	1.40e-4
$I_{\text{u}}[\text{kgm}^2]$	4.34e-1	4.34e-1	4.34e-1
$K_{\text{s}}[\frac{\text{N m}}{\text{rad}}]$	5.52e+2	5.62e+1	1.20e+4
N	-160	-160	-160
$B_{\text{r}}^*[\frac{\text{N m s}}{\text{rad}}]$	9.04e-4	9.04e-4	9.04e-4
$B_{\text{s}}^*[\frac{\text{N m s}}{\text{rad}}]$	1.37e+0	7.24e-1	2.16e+1
$B_{\text{u}}^*[\frac{\text{N m s}}{\text{rad}}]$	1.03e-1	1.03e-1	1.03e-1

as well as the spring stiffness K_{s} were determined by CAD data and dedicated measurements. The damping values B_{u}, B_{s} and B_{r} were experimentally identified; see starred variables in Table V.

A. Parameter Identification

This section shall validate the modelling from Sec. III-A. Furthermore, we want to identify the unknown damping values B_{u}, B_{s} and B_{r}. Therefore, we measure $\left|T(j\omega)\right|$ for the DEA configurations listed in Table V and compare the results to our model which uses a priori known system parameters.

1) Experiment Process: Goal of the experiment process is to obtain frequency response data from 0.5 Hz to 250 Hz to identify the damping values in an optimization similar to [56]. Since the frequency window is quite wide, it is hard to obtain data on all frequencies with a single measurement. We therefore apply multiple overlapping chirp signals from 0.5 Hz to 250 Hz on τ_{m} and measure the torque response on τ_{u}. Each individual chirp signal is applied three times.

The commonly used Fast-Fourier-Transform results in gain data for equally spaced frequency bins. This overemphasizes the high frequency behavior. E.g. for a spacing of 10 Hz the whole domain from 1 Hz to 10 Hz is covered by 2 data points while from 10 Hz to 100 Hz 9 data points are available. We therefore use the Goertzl algorithm [57] which allows to specify the frequencies for which the gain is calculated at the cost of more computation time. We use a precomputed logarithmically spaced frequency vector with growing distance between the frequency bins. The usage of the Goertzl algorithm further allows us to use frequency dependent Henning window width. This minimizes effects of the start and the end of the discontinuous single measurements. The resulting gain on each frequency is plotted with a dot in Fig. 10. Overlapping dots on the same frequency represent results on different chirp signals.

2) Identification: At this point we use the MATLAB *fmincon* algorithm with the goal to minimize the difference of simulated frequency response $\left|T(j\omega)\right|$ with the measurement by modifying the damping values similar to [56] where we enforce the same damping values B_{r} and B_{u} in all configurations.

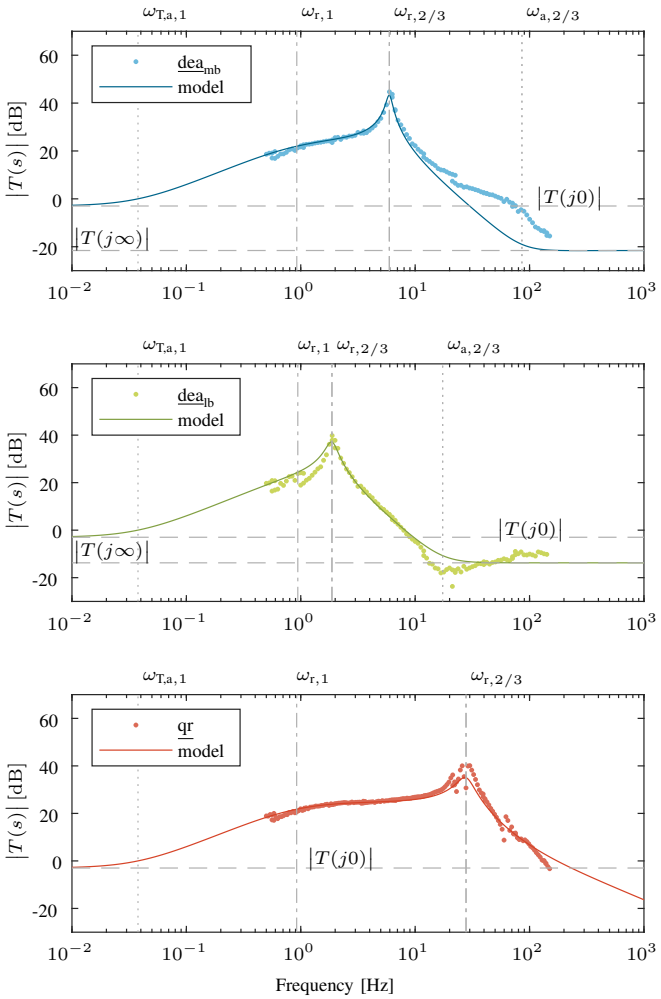

Fig. 10. Gain over frequency of the Transmissibility $T(s)$ for DEA configurations listed in V from 0.5 Hz to 250 Hz. Measurements are denoted with dots and model predictions with a solid line. **Top**: For the $\underline{\text{dea}}_{\text{mb}}$configuration model and measurement matches closely up until $\omega_{\text{r,2/3}}$. We speculate that deviations for higher frequencies are caused by nonlinear stick-slip effects. **Middle**: For the $\underline{\text{dea}}_{\text{lb}}$configuration model and measurement matches closely for the whole frequency range. **Bottom**: For the $\underline{\text{qr}}$ configuration model and measurement matches closely for the whole frequency range, but the peak value of $|T(\omega_{\text{r,2/3}})|$ where we speculate that this is caused by nonlinearity of the stiffness for this configuration.

3) Results: In this subsection we will describe the experimental results. Our interpretations are in the next subsection. The identified damping values are given in Table V. The resulting model-based estimations are presented in Table VI and plotted in Fig. 10. In comparison to the measured frequency response we conclude that from 0.5 Hz to about 110 Hz the estimations match the predicted behavior closely. Above 110 Hz the measured Transmissibility of the $\underline{\text{dea}}_{\text{mb}}$ configuration is higher than predicted. For the $\underline{\text{dea}}_{\text{lb}}$ configuration this effect is not present, and the high frequency gain can be reached. The $\underline{\text{dea}}_{\text{lb}}$ shows an antiresonance peak at $\omega_{\text{a,2/3}}$ in the measurements but not in the model. The resonance peak for the $\underline{\text{qr}}$ configuration in the model is below the measurements. Corner frequencies and their approximations from II are given in Table VI

TABLE VI
CORNER FREQUENCY ESTIMATES

[Hz]	$\underline{\text{dea}}_{\text{mb}}$		$\underline{\text{dea}}_{\text{lb}}$		$\underline{\text{qr}}$	
$\omega_{\text{r},1}$	9.23e-1		9.42e-1		9.21e-1	
$\tilde{\omega}_{\text{r},1}$	1.03e+0	11 %	1.03e+0	9.0 %	1.03e+0	12.0 %
$\hat{\omega}_{\text{r},1}$	0	-100 %	0	- 100 %	0	-100 %
$\omega_{\text{r},2/3}$	5.95e+0		1.87e+0		2.78e+1	
$\tilde{\omega}_{\text{r},2/3}$	5.66e+0	-4.8 %	1.80e+0	-3.8 %	2.65e+1	-4.9 %
$\hat{\omega}_{\text{r},2/3}$	5.96e+0	0.1 %	1.90e+0	1.1 %	2.78e+1	0.0 %

[Hz]	$\underline{\text{dea}}_{\text{mb}}$		$\underline{\text{dea}}_{\text{lb}}$		$\underline{\text{qr}}$	
	$T(s)$	$R(s)$	$T(s)$	$R(s)$	$T(s)$	$R(s)$
$\omega_{\text{a},1}$	3.78e-2	1.03e+0	3.78e-2	1.03e+0	3.78e-2	1.03e+0
$\omega_{\text{a},2/3}$	8.58e+1	8.58e+1	1.74e+1	1.74e+1	-	-

4) Evaluation: The result shows that our model matches the measured behavior for $\omega < \omega_{\text{r},2/3}$. The high frequency gain of the $\underline{\text{dea}}_{\text{mb}}$ configuration is not captured in contrast to that of the $\underline{\text{dea}}_{\text{lb}}$ configuration, which matches the model. We speculate that for the $\underline{\text{dea}}_{\text{mb}}$ configuration an additional dynamic for high frequencies exists, since the same deviation is not present for other configurations. We speculate that it could be a stick-slip effect in combination with the high pretension for the $\underline{\text{dea}}_{\text{mb}}$ configuration. An effect of the high deviation at $\omega_{\text{a},2/3}$ for the $\underline{\text{dea}}_{\text{mb}}$ configuration is that a high value for B_{s}^* is identified, since a small value would emphasize the antiresonance peak. This could explain the higher value of B_{s}^* for the $\underline{\text{dea}}_{\text{mb}}$ configuration in comparison to the $\underline{\text{dea}}_{\text{lb}}$ configuration. We further speculate that in turn a too low value of B_{u}^* is identified to for an overall similarly damped $\underline{\text{dea}}_{\text{mb}}$ configuration. As such for the $\underline{\text{dea}}_{\text{lb}}$ and $\underline{\text{qr}}$ configuration B_{s}^* is overemphasized. This is supported by the fact, that with lower values of B_{s}^* our model would approximate the antiresonance peak of the $\underline{\text{dea}}_{\text{lb}}$ configuration and the resonance peak of the $\underline{\text{qr}}$ configuration better. Furthermore, the value for B_{s}^* for the $\underline{\text{qr}}$ configuration is two magnitudes higher than for $\underline{\text{dea}}_{\text{lb}}$ configuration, which seems unrealistic.

From the measurements on the $\underline{\text{dea}}_{\text{lb}}$ configuration we conclude that the high frequency gain can be tuned by adjusting the spring inertia, and that (20) is valid.

In our design hypothesis we speculated that the damping of heavy load bearings cannot be neglected. However, the evaluation of the corner frequencies and their approximations in Table VI shows, that both the approximation with high gear ratio and the approximation with no damping yield similar results for the resonance frequencies $\omega_{\text{r},i}$. We want to note that is also valid for manually tuned values of B_{s}^* and B_{u}^*.

The identification of the additional dynamic effect that appears in the $\underline{\text{dea}}_{\text{mb}}$ configuration measurement with additional modified experiments and detailed time domain evaluation remains future work. As a result of this additional dynamic our parameter identification procedure likely overemphasizes B_{s}^* over B_{u}^* in all experiment configurations.

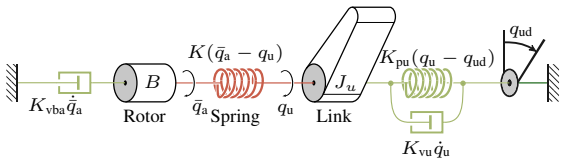

Fig. 11. Closed-loop behavior realized by the ESπ controller assuming SEA dynamics, adapted from [59] Figure 2. The constant K_{pu} denotes the stiffness of the virtual spring between the actual link and the desired link position q_{ud}. The variables K_{vu} and K_{vba} represent virtual damping constants. Note that the rotor coordinate q_{r} is reflected through the gearbox and a coordinate transformation is applied resulting in the virtual motor coordinate $\bar{q}_{\text{a}}$. The motor inertia B and the physical spring stiffness K are obtained by reflecting I_{r} and K_{s} through the gearbox, respectively: $B = N^2 I_{\text{r}}$, $K = \frac{N^2}{(N-1)^2} K_{\text{s}}$.

B. Shaping the Interaction Stiffness

Since interaction with the environment is crucial for many robotic applications, we show that state-of-the-art joint impedance controllers for the $\underline{\text{dea}}_{\text{mb}}$ and $\underline{\text{qr}}$ configuration are applicable. However, a detailed investigation of which control approaches are most suitable remains future work.

In this subsection, we show that the controllers can realize two desired interaction stiffnesses, meaning the static relationship between external link-side torque τ_{ext} and link position q_{u}. Sec. VI-C demonstrates the damping behavior after a harsh impact.

1) Controllers: For each configuration ($\underline{\text{dea}}_{\text{mb}}$ and $\underline{\text{qr}}$, see Table V) one impedance control approach is implemented. Both controllers described below allow motor inertia shaping, but for simplicity the motor inertia remains unchanged for the experiments. Furthermore, gravity compensation that both controllers offer is obsolete in these experiments since the link moves in a horizontal plane. In addition to the impedance controllers, a momentum-based motor friction compensation [58] is implemented for both setups.

The ESπ controller [59] based on [60] assumes SEA dynamics and adopts impedance control techniques to articulated soft robots with high actuator elasticity. Therefore, it is implemented for the highly elastic $\underline{\text{dea}}_{\text{mb}}$ configuration, see Table V. Based on a control input and a motor coordinate transformation and assuming SEA dynamics it realizes the closed-loop behavior that is depicted in Fig. 11.

The virtual damping constants are chosen as $K_{\text{vu}} = 2\xi_{\text{u}}\sqrt{I_{\text{u}} K_{\text{pu}}}$ and $K_{\text{vba}} = 2\xi_{\text{ba}}\sqrt{BK}$. The controller parameters (tuned manually) are: $\xi_{\text{ba}} = 0.3, \xi_{\text{u}} = 0.7$. For the desired interaction stiffness two values are used as explained below: $K_{\text{pu}} = 200\,\text{Nm/rad}$ and $K_{\text{pu}} = 400\,\text{Nm/rad}$.

The LWR joint impedance controller [61] was developed for lightweight robots with significantly higher actuator stiffness values than the ones of our highly elastic configuration. Therefore, it is used for the experiments with the $\underline{\text{qr}}$ configuration, see Table V. The controller realizes a motor-side virtual damper and guarantees a desired interaction stiffness limited to be smaller than the physical actuator stiffness. Note that this limitation does not apply to the ESπ controller. Following the notation in [61] the LWR joint impedance control parameters (tuned manually) are: $D_\Theta = 2\xi_\Theta\sqrt{BK_{\text{q}_\text{d}}}$ with $\xi_\Theta = 3$ and

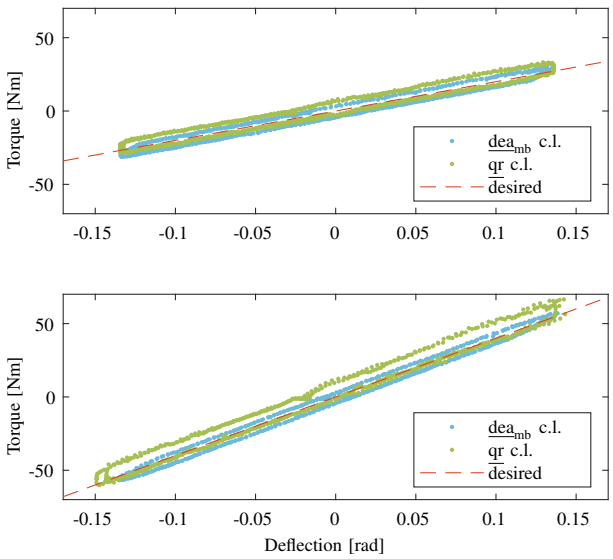

Fig. 12. External link-side torque over link deflection for different system setups. Top: closed-loop (c.l.) behavior for a desired interaction stiffness of 200 Nm/rad. The root mean squared error (rmse) for $\underline{\text{dea}}_{\text{mb}}$ c.l. equals 3.3 Nm and the rmse for $\underline{\text{qr}}$ c.l. equals 3.8 Nm., Bottom: closed-loop (c.l.) behavior for a desired interaction stiffness of 400 Nm/rad. The rmse for $\underline{\text{dea}}_{\text{mb}}$ c.l. equals 3.0 Nm and the rmse for $\underline{\text{qr}}$ c.l. equals 4.8 Nm.

$D_{\text{s}} = 1.65\,\text{Nm/rads}$. For the desired interaction stiffness two values are used as explained below: $K_{\text{q}_{\text{d}}} = 200\,\text{Nm/rad}$ and $K_{\text{q}_{\text{d}}} = 400\,\text{Nm/rad}$.

2) Experiment Process: In order to determine the interaction stiffness, a human user slowly moves the link back and forth while the respective controller is active. Fig. 12 shows the applied torque depending on the link deflection. The torque is measured by the torque sensor and the deflection is the difference between the actual link position obtained by the link position sensor and the constant desired link position. The experiment was conducted for two different desired interaction stiffnesses, 200 Nm/rad and 400 Nm/rad, for each setup.

3) Evaluation and Results: Fig. 12 shows a linear relation between the external torque exerted on the link and the link deflection. Furthermore, the experimental data closely approximates (see root mean squared errors) the respective desired interaction stiffness shown by a red dashed line. The hysteresis is mainly due to the not perfectly compensated motor-side friction. Scaling the motor inertia down via motor inertia shaping can reduce this hysteresis since it also decreases the influence of motor-side friction in the closed-loop dynamics [59], [61].

C. Impact Response

In this experiment we want to show that the physical system behaves analogous to our model for the $\underline{\text{dea}}_{\text{mb}}$, $\underline{\text{dea}}_{\text{lb}}$ and $\underline{\text{qr}}$ configurations which are subjected to impacts. Furthermore, we want to demonstrate damping behavior of the implemented impedance controllers. Finally, we want to evaluate the usefulness of the introduced torque estimates τ_{init}, $\hat{\tau}_{\text{peak}}$ and $\tilde{\tau}_{\text{peak}}$.

1) Experiment Process: Our experiment setup consists of horizontally mounted DEA with attached link as visible in Fig. 9 and gravity driven pendulum with a length of $l_{\text{g}} = 850\,\text{mm}$, total mass of $3.8\,\text{kg}$ and an inertia of $I_{\text{g}} = 2.1\,\text{kgm}^2$. We assume a gravitational constant of $g = 9.81\,\text{m/s}^2$. We measure the pendulum deflection before release α_{p} with a visual scale. The pendulum hits the link distanced by $l_{\text{u}} = 0.38\,\text{m}$ from the actuator axis.

The pendulum is both released and caught manually for this experiment. For all configurations we test two different setups, the open-loop (o.l) setup with lifted brakes and no controller running as well as the closed-loop (c.l.) setups where the impedance controller from the previous section are used with the same parametrization. The different impact experiments are summarized in the top part of Table VII. Every experiment was executed three times.

For evaluation the constant torque sensor offset is subtracted from the data. All measurements are then synchronized by the last noise induced zero crossing before the first torque maximum.

2) Impact Torque Prediction: To compare the torque measurements with our predictions we compute the transmitted rotational impulse after impact τ'_{coll} with the process detailed in the Appendix Sec. VIII-A.

The impact velocity of the pendulum $\dot{q}_{\text{g}}$ follows from the assumption of equal kinetic energy before impact and potential energy after release of the pendulum. In impact direction $\boldsymbol{n} = [1, 0, 0]^T$ the respective Jacobians at time of impact evaluate to $J_{\text{u}} = l_{\text{u}}$ and $J_{\text{g}} = -l_{\text{g}}$. Equation (74) determines $I_{\text{coll}} = I_{\text{u}} I_{\text{g}} / (I_{\text{u}}\, {l_{\text{g}}}^2 + I_{\text{g}}\, {l_{\text{u}}}^2)$. With $\Delta v = l_{\text{g}} \dot{q}_{\text{g}}$ and $e = 1$ we compute τ'_{coll} from (73). For our experimental configurations the approximated post-impact velocities have the same sign. Since the pendulum swings back towards its original position, we assume a second impact. To calculate properties of the second impact, we simulate link movement and pendulum movement.

We determine Δt from the width of the initial oscillations in our experimental data as $\Delta t = 3\,\text{ms}$ which is equivalent to $c = 2e6\,\text{N/m}$.

From τ'_{coll} and Δt we compute $\tau_{\text{u,coll}}(t)$ as well as the approximated expressions $\hat{\tau}_{\text{peak}}(t)$ and $\tilde{\tau}_{\text{peak}}(t)$. Estimated values are given for all experiments at the bottom part of Table VII.

3) Results: The resulting torque measurements together with the simulations are shown in Figures 13 and 14. We use the maximum torque in the measurement as peak torque τ_{peak} and the first local maximum as initial torque value τ_{init}. Both are summarized in the middle part of Table VII where they are normalized by τ_{coll}.

Compared to our simulation and description from Sec. III-B the sine-like oscillation starts with a small delay comparable to Δt. Furthermore, the second impact is not clearly visible in most measurements except for small impacts on the $\underline{\text{dea}}_{\text{lb}}$ setup and closed-loop $\underline{\text{dea}}_{\text{mb}}$ setup in 13. In both cases a disturbance is visible at a similar time of the second impact prediction. For all other experiments the decreasing half of the first sine wave is deformed by a plateau ($\underline{\text{dea}}_{\text{mb}}$ setup) or the peak of the sine wave is widened ($\underline{\text{qr}}$ setup). After the impact small overlaid oscillations can be observed. For the $\underline{\text{qr}}$ setup we set $\tau_{\text{init}} = 0$

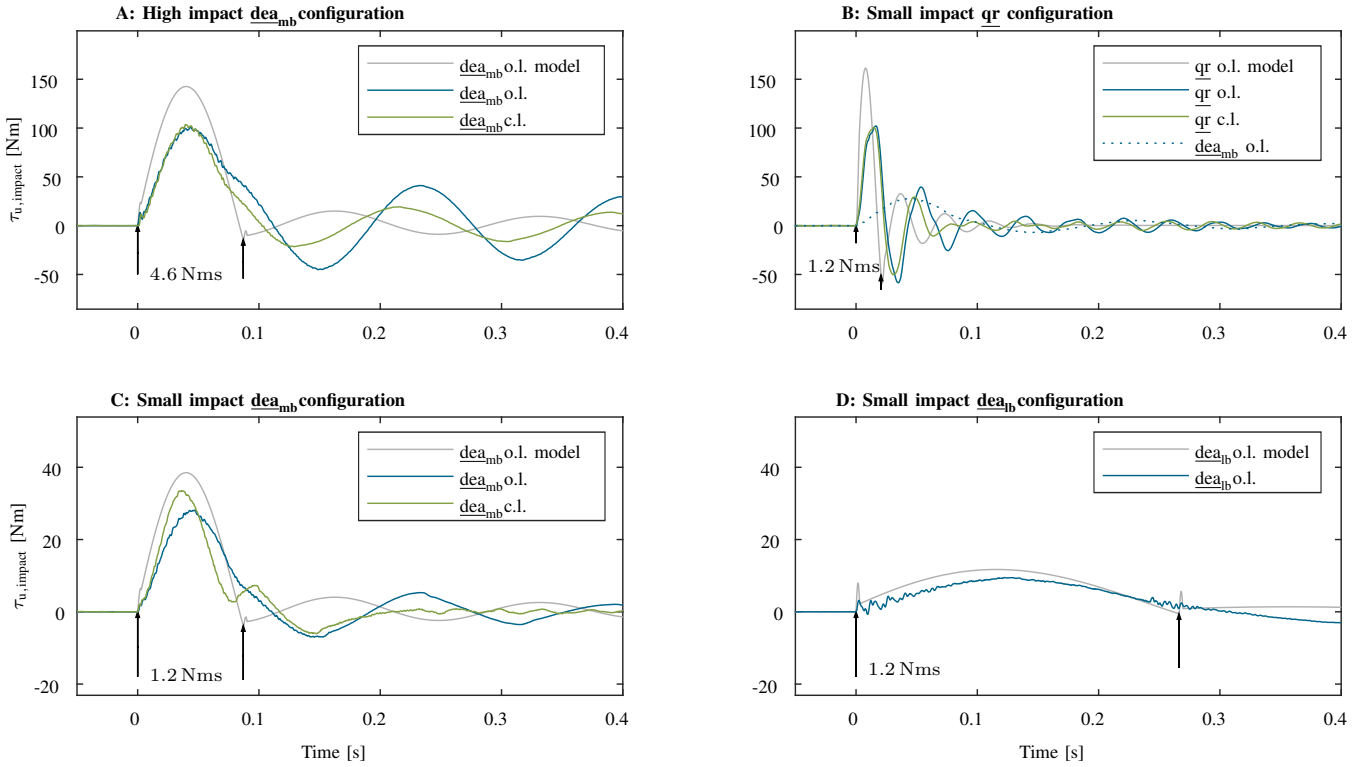

Fig. 13. Measurements and model-based predictions of the impact-related gear torque $\tau_{\mathrm{u,impact}}$. The open-loop behavior of the system with open brakes and no controller is shown in blue. The closed-loop behaviors are shown in green. For the $\underline{\mathrm{dea}}_{\mathrm{mb}}$ and $\underline{\mathrm{dea}}_{\mathrm{lb}}$ configuration the open-loop model (41) is shown in gray. **A**: The impact pendulum is deflected by $80°$ and exerts a torque shock of about $4.6\,\mathrm{Nms}$ on the $\underline{\mathrm{dea}}_{\mathrm{mb}}$ setups. **B**: Pendulum deflection of $20°$ and torque shock of $1.2\,\mathrm{Nms}$ on the $\underline{\mathrm{qr}}$ setups and the $\underline{\mathrm{dea}}_{\mathrm{mb}}$ open-loop setup. **C**: Pendulum deflection of $20°$ and torque shock of $1.2\,\mathrm{Nms}$ on the $\underline{\mathrm{dea}}_{\mathrm{mb}}$ system. **D**: Pendulum deflection of $20°$ and torque shock of $1.2\,\mathrm{Nms}$ on the $\underline{\mathrm{dea}}_{\mathrm{lb}}$ system

TABLE VII
IMPACT EXPERIMENT. A: PARAMETERS, B: MEASUREMENTS AND C: ESTIMATIONS

A: Experiment Parameters	configuration		$\underline{\mathrm{dea}}_{\mathrm{mb}}$		$\underline{\mathrm{dea}}_{\mathrm{mb}}$		$\underline{\mathrm{dea}}_{\mathrm{mb}}$		$\underline{\mathrm{dea}}_{\mathrm{lb}}$		$\underline{\mathrm{qr}}$	
	α_{p}	[°]	80		60		20		20		20	
	τ'_{coll}	[Nms]	4.6		3.6		1.2		1.2		1.2	
B: Normalized measurement	τ_{init} $1\,\mathrm{Nms}/p_{\mathrm{r},1}$	[Nm]	2.85		2.51		1.58		1.58		0	
	τ_{peak} $1\,\mathrm{Nms}/p_{\mathrm{r},1}$	[Nm]	21.9		22.3		22.7		7.65		82.4	
C: Estimation for $\tau'_{\mathrm{coll}} = 1\,\mathrm{Nms}$ with deviation from measurement	τ_{init}	[Nm]	4.17	46 %	4.17	66 %	4.17	163 %	6.23	153 %	0	0 %
	τ_{peak}	[Nm]	31.6	44 %	31.6	42 %	31.6	39 %	9.82	14 %	156	68 %
	$\tilde{\tau}_{\mathrm{peak}}$	[Nm]	33.2	52 %	33.2	49 %	33.2	46 %	10.5	37 %	156	89 %
	$\hat{\tau}_{\mathrm{peak}}$	[Nm]	33.7	54 %	33.7	51 %	33.7	49 %	10.4	36 %	166	101 %

since there is no intermediate torque level in the measurement. Fig. 13 allows to compare the closed-loop and the open-loop behavior after impact. In all experiments both τ_{init} and τ_{peak} are comparable or higher for the closed-loop setups. When comparing different iterations of the same experiment as in Fig. 14, very little variation can be observed. Not only does the general behavior hardly change, the overlaid oscillations stay in phase at least until the decreasing torque plateau.

4) Evaluation: From Figures 13 and 14 we conclude that (40) provides a conservative approximation of $\tau_{\mathrm{u,coll}}(t)$, where the predicted torque is higher than the measured torque. Some restrictions apply. Firstly, we are unable to predict the delay in the measurements, and secondly the simulation and prediction of the second impact leads to great errors in the overall response. Third, the model fails to predict the small overlaid oscillations. Finally, the plateau in the first sine wave can only be partially explained with a second impact.

We speculate, that with a correct prediction of the delay and less conservative approximation on the transmitted impulse τ'_{coll} the simulation would be able to approximate the post-impact response more precisely. Some mechanisms could be candidates to cause the delay, such as stick-slip effects and nonlinearities in the springs or harmonic drive. We have deliberately left out these effects, disregarded more detailed contact models that could improve the estimation on τ'_{coll} in Sec. II and consider a detailed investigation future work.

The observation, that the first half sine wave $\tau_{\mathrm{u,coll}}(t)$ is similar or higher for closed-loop systems shows that the initial impact response is not reduced by state-of-the-art impedance controllers which do not have this control objective. To re-

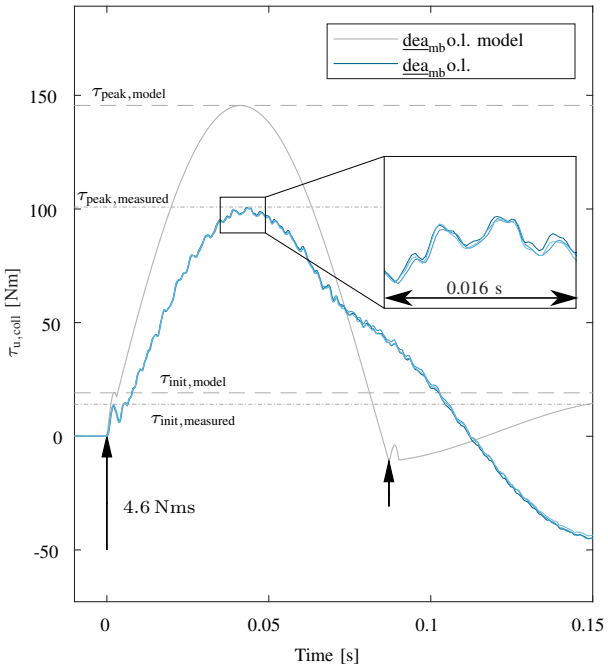

Fig. 14. Closeup on the measurements of the impact-related gear torque $\tau_{\text{u,impact}}$ from Fig. 13. The behavior of the open-loop model is shown in gray. Three different measurements on the open-loop $\underline{\text{dea}}_{\text{mb}}$ configurations with the same torque shock of about $4.1\,\text{Nms}$ with an impact pendulum of $80°$ are shown in blue colors. The measurements stay in phase until the second projected impact.

duce the impact torque specialized reaction strategies [62] or a proper mechanical design is needed. Even though the controllers were only roughly tuned to dampen post-impact vibrations, their usefulness can be observed with the reduction of successive peaks compared to the open-loop configurations.

Another observation is, that the $\underline{\text{qr}}$ configuration experiences about 3.6 times higher τ_{peak} than the $\underline{\text{dea}}_{\text{mb}}$ configuration. This demonstrates that differential elasticity drastically improves impact robustness, similar to the findings of [22].

Evaluation of the predicted torques as in Table VII further shows that for the presented differential elastic configurations, we were able to give a conservative prediction of the maximum measured impact torque with the approximate expressions on τ_{init}, $\tilde{\tau}_{\text{peak}}$ and $\hat{\tau}_{\text{peak}}$.

In our view this is sufficient to allow the usage of these expressions as design criteria.

VII. Conclusion

In this article we presented a design guide for DEAs that supports the robot designer in choosing the proper stiffness, damping and inertia parameters for their robotic application in order to achieve a desired performance and robustness. Therein, we proposed to use the open-loop torque bandwidth of the actuator as measure of performance and the impact-related gear torque as measure of robustness. To ease the computation, we have introduced some simplifying assumptions, one for DEAs with small damping values and one for DEAs with high gear ratios as commonly used for robotic actuators. Regarding the open-loop torque transfer function, we have provided a parameter sweep to visualize the effect of spring-side inertia, stiffness and damping on the gain of the Transmissibility. To validate our formulas, we designed an experimental testbed based on a highly adaptable DEA. As additional features, the DEA provides a torque sensor at the output of the gears, easily exchangeable springs and locking pins that allow to convert our DEA from a highly elastic into a quasi-rigid configuration. Using a frequency domain system identification, we have verified the derived formulas to describe the bandwidth of the actuator. In the same experiment, we verified the prediction of the finite high-frequency gain, although it is too low in our specific case to have a practical impact. However, the experimental verification and prediction of this DEA property is important for designs where spring-side and link-side inertia are closer in size which results in larger high frequency gains. In addition, we implemented state-of-the-art impedance controllers and successfully demonstrated in different experiments their ability to shape the interaction stiffness as well as the damping behavior for our highly elastic DEA and the quasi-rigid setup.

Furthermore, our model predicts the expected impact torque sufficiently well to grant the choice of physical stiffness, which is the most influential parameter to trade off open-loop torque bandwidth and robustness to impact-related gear torque.

In conclusion, we were able to show that the mathematical descriptions provided can be used effectively in the design process of differential elastic actuators to trade-off in between performance and robustness.

In the future, we will investigate the difference in measured link-side torque and model predictions using more detailed impact and gearbox models. Subsequently, we will experimentally verify and exploit DEA behavior with high spring-side damping. Furthermore, we will integrate several actuators in a rover suspension system and apply the design guide in this application.

VIII. Appendix

A. Model

Sec. II-B introduces the used collision model but omits a derivation for multi-link systems. This section derives a worst-case transmitted joint-space impulse τ'_{coll} on the actuator at joint l, when two multi-link systems $k \in \{\text{o}, \text{p}\}$ with n_k links collide at a time $t = 0$. A simple spring-mass contact model approximates the collision duration Δt and the maximum collision force $\tau_{\text{ext,coll,max}}$.

If not otherwise stated, quantities have scalar values. Dependencies are omitted once understood.

We consider joint-space coordinates $\boldsymbol{q}_k(t) \in \mathbb{R}^{n_k}$, inertia matrix $\boldsymbol{I}_k(\boldsymbol{q}_k) \in \mathbb{R}^{n_k \times n_k}$, vector of Coriolis and potential forces $\boldsymbol{h}_k(\boldsymbol{q}_k, \dot{\boldsymbol{q}}_k) \in \mathbb{R}^{n_k}$ with a joint-space actuation force $\boldsymbol{\tau}_{act,k}(t) \in \mathbb{R}^{n_k}$ and joint-space non-conservative forces $\boldsymbol{\tau}_{\text{nk},k}(t) \in \mathbb{R}^{n_k}$.

The respective equation of motion then reads,

$$\boldsymbol{I}_k(\boldsymbol{q}_k)\ddot{\boldsymbol{q}}_k + \boldsymbol{h}_k(\boldsymbol{q}_k, \dot{\boldsymbol{q}}_k) = \boldsymbol{\tau}_{act,k}(t) + \boldsymbol{\tau}_{\text{nk},k}(t). \tag{70}$$

The Jacobian $\boldsymbol{J}_k(\boldsymbol{q}_k) \in \mathbb{R}^{3\times n_k}$ relates $\dot{\boldsymbol{q}}_k$ to Cartesian velocities $\boldsymbol{v}_k(\boldsymbol{q}_k, \dot{\boldsymbol{q}}_k) \in \mathbb{R}^3$ at a position $\boldsymbol{r}_k(\boldsymbol{q_k}) \in \mathbb{R}^3$ as $\boldsymbol{v}_k = \boldsymbol{J}_k\dot{\boldsymbol{q}}_k$ and external Cartesian forces $\boldsymbol{f}_{\text{nk},k}(t) \in \mathbb{R}^3$ as $\boldsymbol{\tau}_{\text{nk},k} = \boldsymbol{J}_k^T\boldsymbol{f}_{\text{nk},k}$. We define $\boldsymbol{J}_{k,i}$ as the i's column of $\boldsymbol{J}_k$.

For a collision at position $\boldsymbol{r}_\text{o}(\boldsymbol{q}_\text{o}(0)) = \boldsymbol{r}_\text{p}(\boldsymbol{q}_\text{p}(0))$ we define the contact normal $\boldsymbol{n}$ from system o as $\boldsymbol{n} = \boldsymbol{n}_\text{o} = -\boldsymbol{n}_\text{p}$ and the velocity difference

$$\Delta v = \Delta \boldsymbol{v}^T\boldsymbol{n} = \left(\boldsymbol{v}_\text{o}(0) - \boldsymbol{v}_\text{p}(0)\right)^T\boldsymbol{n}. \tag{71}$$

Generally, collisions transmit normal and tangential forces. We assume that $\boldsymbol{n}$ is parallel to $\Delta\boldsymbol{v}$

$$\boldsymbol{n} = \Delta\boldsymbol{v}/\|\Delta\boldsymbol{v}\|. \tag{72}$$

This choice maximizes $\boldsymbol{f}_\text{coll}$ with the benefit that no tangential forces are present and friction can be neglected. Furthermore, the collision force $\boldsymbol{f}_\text{coll} = \boldsymbol{f}_\text{nk,o} = -\boldsymbol{f}_\text{nk,p}$ acts along a contact normal $\boldsymbol{n}$ with $\boldsymbol{f}_\text{coll} = \boldsymbol{n}f_\text{coll}$.

When assuming rigid-body contact dynamics the transmitted rigid-body impulse $\boldsymbol{f}'_\text{coll,rb} \in \mathbb{R}^3$ is a function of Δv, the rigid-body contact inertia $I_\text{coll,rb}$ in the direction $\boldsymbol{n}$ and the coefficient of restitution $e \in [0, 1]$ [63],[64]

$$\begin{aligned}\boldsymbol{f}'_\text{coll,rb} =& f'_\text{coll,rb}\boldsymbol{n}\\ =& -(1+e)\Delta v I_\text{coll,rb}\boldsymbol{n}.\end{aligned} \tag{73}$$

where $I_\text{coll,rb}$ is computed as the reciprocal sum of the contact inertia

$$I_\text{coll,rb} = \left(\boldsymbol{n}^T\left(\boldsymbol{J}_\text{o}{\boldsymbol{I}_\text{o}}^{-1}\boldsymbol{J}_\text{o}^T + \boldsymbol{J}_\text{p}{\boldsymbol{I}_\text{p}}^{-1}\boldsymbol{J}_\text{p}^T\right)\boldsymbol{n}\right)^{-1}. \tag{74}$$

Furthermore, the rigid-body contact duration $\Delta t_\text{rb} = 0$ and thus the rigid-body collision force $\boldsymbol{f}_\text{coll,rb}(t)$ is infinite. It can be described with the Dirac-delta function $\delta(t)$ as

$$\boldsymbol{f}_\text{coll,rb}(t) = \boldsymbol{f}'_\text{coll,rb}\delta(t). \tag{75}$$

A simple spring-mass contact model allows usage of a finite valued $f_\text{coll}(t)$. The model, visualized on the top left of Fig. 1, introduces a contact stiffness c and contact inertia I_coll. Contact motion is sinusoidal in time, where Δt is a half period and is given with the maximum collision force $f_\text{coll,max}$ [50] as,

$$\Delta t = \pi\sqrt{I_\text{coll}/c}, \tag{76}$$

$$f_\text{coll,max} = -c\Delta v\Delta t/\pi. \tag{77}$$

The respective contact force $f_\text{coll}(t)$ can be written with the Heaviside function $\sigma(t)$ for $t > 0$

$$f_\text{coll}(t) = f_\text{coll,max}\left(1 - \sigma(t - \Delta t)\right)\sin(\tfrac{\pi}{\Delta t}t). \tag{78}$$

We ask that the transmitted impulse is equivalent in the rigid-body case and the spring-mass model

$$\begin{aligned}f'_\text{coll} =& \int f_\text{coll}(t)\,\mathrm{d}t = -2\Delta v I_\text{coll}\\ =& f'_\text{coll,rb}.\end{aligned} \tag{79, 80}$$

With no dissipation mechanism in the contact model we identify $e = 1$ and from (79)

$$I_\text{coll} = I_\text{coll,rb}. \tag{81}$$

TABLE VIII
DENOMINATOR SIMPLIFICATION

	$D(s)$	$\tilde{D}(s)$	$\hat{D}(s)$
d_3	$((N-1)^2 I_\text{r}+I_\text{s})I_\text{u}$ $+I_\text{r}N^2 I_\text{s}$	$N^2(I_\text{u}I_\text{r}+I_\text{r}I_\text{s})$	$(N-1)^2 I_\text{r}I_\text{u}$ $+I_\text{r}I_\text{s}N^2+I_\text{s}I_\text{u}$
d_2	$(N-1)^2(B_\text{u}I_\text{r}+B_\text{r}I_\text{u})$ $+(I_\text{r}N^2+I_\text{u})B_\text{s}$ $+I_\text{s}(B_\text{r}N^2+B_\text{u})$	$B_\text{r}N^2(I_\text{u}+I_\text{s})$ $+I_\text{r}N^2(B_\text{u}+B_\text{s})$	0
d_1	$((N-1)^2 B_\text{r}+B_\text{s})B_\text{u}$ $+B_\text{r}B_\text{s}N^2$ $+K_\text{s}(I_\text{r}N^2+I_\text{u})$	$B_\text{r}N^2(B_\text{u}+B_\text{s})$ $+I_\text{r}N^2K_\text{s}$	$K_\text{s}(I_\text{r}N^2+I_\text{u})$
d_0	$K_\text{s}(B_\text{r}N^2+B_\text{u})$	$B_\text{r}K_\text{s}N^2$	0

Park et al.[65] use a similar collision assumption but perform a time continuous simulation and obtain similar results.

We link our Cartesian results to the linear model with $\tau_\text{ext} = \tau_{\text{nk,o},l}$. By neglecting joint movement during Δt we compute

$$\tau_\text{ext,coll}(t) = \boldsymbol{J}_{\text{o},l}^T(\boldsymbol{q}_\text{o}(0))\boldsymbol{n}f_\text{coll}(t), \tag{82}$$

$$\tau'_\text{coll} = \boldsymbol{J}_{\text{o},l}^T(\boldsymbol{q}_\text{o}(0))\boldsymbol{n}f'_\text{coll}, \tag{83}$$

$$\tau_\text{ext,coll,max} = \boldsymbol{J}_{\text{o},l}^T(\boldsymbol{q}_\text{o}(0))\boldsymbol{n}f'_\text{coll,max} = \frac{\pi\tau'_\text{coll}}{2\Delta t}. \tag{84}$$

We suggest calculating τ'_coll under assumption of rigid-body dynamics and to use a worst-case approximation of Δt for a worst-case estimate on $\tau_\text{ext,coll,max}$.

In Sec. II-A we derive $T(s)$. To do this we transfer (4) to the Laplace domain with abbreviations $P_\text{r}(s)$, $P_\text{s}(s)$, $P_\text{u}(s)$ and arrive at

$$q_\text{r}(s) = P_\text{r}(s)\left(\tau_\text{m}(s) - \tfrac{1}{N-1}\tau_\text{s}(s)\right), \tag{85}$$

$$q_\text{s}(s) = -P_\text{s}(s)\tau_\text{s}(s), \tag{86}$$

$$q_\text{u}(s) = P_\text{u}(s)\left(\tau_\text{ext}(s) + \tfrac{N}{N-1}\tau_\text{s}(s)\right). \tag{87}$$

Inserting (1),(85) and (87) in (86) yields

$$\frac{NP_\text{u}(\frac{N\tau_\text{s}}{N-1} + \tau_\text{ext})}{N-1} - \frac{P_\text{r}(\tau_\text{r} - \frac{\tau_\text{s}}{N-1})}{N-1} = -P_\text{s}\tau_\text{s}. \tag{88}$$

By solving (88) for τ_s, inserting $\tau_\text{u} = -\frac{N}{N-1}\tau_\text{s}$ and setting $\tau_\text{ext}(s) = 0$ we arrive at (5).

B. Analysis

Sec. III-A introduce two approximations for both $T(s)$ and $R(s)$. To apply them we reduce both $T(s)$ and $R(s)$ to minimal order as $T(s) = \frac{\text{Num}(T(s))}{\text{Den}(T(s))}$ and $R(s) = \frac{\text{Num}(R(s))}{\text{Den}(R(s))}$ with the same denominator $D(s) = \text{Den}(R(s)) = \text{Den}(T(s))$ of order three, $D(s) = d_3s^3+d_2s^2+d_1s+d_0$. Table VIII shows factors d_i of the denominator $D(s)$ for each simplification.

In Sec. III-B we omit presentation of the impact torque for the assumption of a high gear ratio $\tilde{\tau}_\text{u,coll}(t)$. With (16) we approximate a with $\hat{a}$

$$\hat{a} = \frac{I_\text{s}}{(I_\text{u} + I_\text{s})}, \tag{89}$$

and $b(t)$ with $\tilde{b}(t)$

$$\tilde{b}(t) = \tilde{b}_1(\mathrm{e}^{t\tilde{p}_2} + \mathrm{e}^{t\tilde{p}_3}) + \tilde{b}_2(\mathrm{e}^{t\tilde{p}_2} - \mathrm{e}^{t\tilde{p}_3}) \tag{90}$$

where

$$\tilde{p}_2 = -\frac{B_\mathrm{u}+B_\mathrm{s}-\sqrt{(B_\mathrm{u}+B_\mathrm{s})^2-4(I_\mathrm{u}+I_\mathrm{s})K_\mathrm{s}}}{2(I_\mathrm{u}+I_\mathrm{s})},$$
$$\tilde{p}_3 = -\frac{B_\mathrm{u}+B_\mathrm{s}+\sqrt{(B_\mathrm{u}+B_\mathrm{s})^2-4(I_\mathrm{u}+I_\mathrm{s})K_\mathrm{s}}}{2(I_\mathrm{u}+I_\mathrm{s})},$$
$$\hat{b}_1 = \frac{(-B_\mathrm{u}I_\mathrm{s}+I_\mathrm{u}B_\mathrm{s})}{2(I_\mathrm{u}+I_\mathrm{s})^2},$$
$$\hat{b}_2 = \frac{(2I_\mathrm{u}K_\mathrm{s}(I_\mathrm{u}+I_\mathrm{s})-I_\mathrm{u}B_\mathrm{s}B_\mathrm{u}+I_\mathrm{u}B_\mathrm{s}^2+B_\mathrm{u}^2I_\mathrm{s}+B_\mathrm{u}B_\mathrm{s}I_\mathrm{s})}{2\sqrt{(B_\mathrm{u}+B_\mathrm{s})^2-4(I_\mathrm{u}+I_\mathrm{s})K_\mathrm{s}}(I_\mathrm{u}+I_\mathrm{s})^2}.$$

Regarding the peak torque, the condition

$$t_\mathrm{peak} = \arg\left(\dot{b}(t) = 0\right), \tag{91}$$

allows computation of the peak torque τ_peak as,

$$\tau_\mathrm{peak} = b(t_\mathrm{peak})\tau'_\mathrm{coll}, \tag{92}$$

which evaluates with (90)

$$\tilde{\tau}_\mathrm{peak} = \tau'_\mathrm{coll}\frac{2\frac{u_2}{u_3}^{-\frac{B_\mathrm{u}+B_\mathrm{s}+u_1}{2u_1}}K_\mathrm{s}}{u_3(B_\mathrm{u}^2I_\mathrm{s}-B_\mathrm{u}B_\mathrm{s}I_\mathrm{u}+I_\mathrm{u}^2K_\mathrm{s})^{-1}}, \tag{93}$$

where

$$\begin{aligned}
u_1 &= \sqrt{(B_\mathrm{u}+B_\mathrm{s})^2-4(I_\mathrm{u}+I_\mathrm{s})K_\mathrm{s}},\\
u_2 &= B_\mathrm{u}^3I_\mathrm{s}+(-B_\mathrm{s}I_\mathrm{u}+I_\mathrm{s}(u_1+2B_\mathrm{s}))B_\mathrm{u}^2\\
&\quad +(I_\mathrm{u}^2K_\mathrm{s}+(-u_1B_\mathrm{s}-2B_\mathrm{s}^2-I_\mathrm{s}K_\mathrm{s})I_\mathrm{u},\\
&\quad +I_\mathrm{s}(u_1B_\mathrm{s}+B_\mathrm{s}^2-2I_\mathrm{s}K_\mathrm{s}))B_\mathrm{u}\\
&\quad -I_\mathrm{u}(-K_\mathrm{s}(u_1+3B_\mathrm{s})I_\mathrm{u}+u_1\,B_\mathrm{s}^2-I_\mathrm{s}K_\mathrm{s}u_1+B_\mathrm{s}^3-3B_\mathrm{s}I_\mathrm{s}K_\mathrm{s}),\\
u_3 &= B_\mathrm{u}^3I_\mathrm{s}+(-B_\mathrm{s}I_\mathrm{u}-I_\mathrm{s}(u_1-2B_\mathrm{s}))B_\mathrm{u}^2,\\
&\quad +(I_\mathrm{u}^2K_\mathrm{s}+(u_1B_\mathrm{s}-2B_\mathrm{s}^2-I_\mathrm{s}K_\mathrm{s})I_\mathrm{u}\\
&\quad -I_\mathrm{s}(u_1B_\mathrm{s}-B_\mathrm{s}^2+2I_\mathrm{s}K_\mathrm{s}))B_\mathrm{u}\\
&\quad +I_\mathrm{u}(-K_\mathrm{s}(u_1-3B_\mathrm{s})I_\mathrm{u}+u_1\,B_\mathrm{s}^2-I_\mathrm{s}K_\mathrm{s}u_1-B_\mathrm{s}^3+3B_\mathrm{s}I_\mathrm{s}K_\mathrm{s}).
\end{aligned}$$

ACKNOWLEDGMENT

We thank Oliver Eiberger, Florian Schmidt, Andreas Stemmer, Clemens Karl and Benedikt Heinrich as well as our workshops for practical support with providing components of the DLR SARA robot. Furthermore, we thank Josef Reill, Maged Iskandar and Sehoon Oh for their valuable theoretical and practical input regarding controls. We also thank the anonymous referees for their valuable comments that improved the quality of the paper.

We gratefully acknowledge the funding provided by the Helmholtz Association in the sustainability challenge iFOODis KA-HSC-06.

REFERENCES

[1] M. Grebenstein, A. Albu-Schäffer, T. Bahls, *et al.*, "The DLR hand arm system," in *IEEE International Conference on Robotics and Automation (ICRA)*, 2011, pp. 3175–3182.

[2] M. Hutter, C. D. Remy, M. A. Hoepflinger, and R. Siegwart, "High compliant series elastic actuation for the robotic leg ScarlETH," in *International Conference on Climbing and Walking Robots and the Support Technologies for Mobile Machines (CLAWAR)*, 2011.

[3] N. Radford, P. Strawser, K. Hambuchen, *et al.*, "Valkyrie: Nasa's first bipedal humanoid robot," *Journal of Field Robotics*, vol. 32, pp. 397–419, 2015.

[4] M. Hutter, C. Gehring, D. Jud, *et al.*, "ANYmal - a highly mobile and dynamic quadrupedal robot," in *IEEE/RSJ International Conference on Intelligent Robots and Systems (IROS)*, 2016, pp. 38–44.

[5] N. G. Tsagarakis, D. G. Caldwell, F. Negrello, *et al.*, "Walk-man: A high-performance humanoid platform for realistic environments," *Journal of Field Robotics*, vol. 34, no. 7, pp. 1225–1259, 2017.

[6] D. Robinson, J. Pratt, D. Paluska, and G. Pratt, "Series elastic actuator development for a biomimetic walking robot," in *IEEE/ASME International Conference on Advanced Intelligent Mechatronics (AIM)*, 1999, pp. 561–568.

[7] W. Townsend and J. Salisbury, "Mechanical bandwidth as a guideline to high-performance manipulator design," in *IEEE/RSJ International Conference on Intelligent Robots and Systems (IROS)*, vol. 3, 1989, pp. 1390–1395.

[8] G. Pratt and M. Williamson, "Series elastic actuators," in *IEEE/RSJ International Conference on Intelligent Robots and Systems (IROS)*, vol. 1, 1995, pp. 399–406.

[9] M. Lauria, M.-A. Legault, M.-A. Lavoie, and F. Michaud, "Differential elastic actuator for robotic interaction tasks," in *IEEE International Conference on Robotics and Automation (ICRA)*, 2008, pp. 3606–3611.

[10] N. Tsagarakis, M. Laffranchi, B. Vanderborght, and D. Caldwell, "A compact soft actuator unit for small scale human friendly robots," in *IEEE International Conference on Robotics and Automation (ICRA)*, 2009, pp. 4356–4362.

[11] N. A. Paine, "High-performance series elastic actuation," Ph.D. dissertation, University of Texas at Austin, 2014.

[12] J. de Gea Fernández, B. Yu, V. Bargsten, M. Zipper, and H. Sprengel, "Design, modelling and control of novel series-elastic actuators for industrial robots," *Actuators*, vol. 9, no. 1, 2020.

[13] R. Baudisch, "Statischer Ausgleich bei Gelenkrobotern," German, *Feingerätetechnik*, vol. 4, no. 34, 1985.

[14] Y. W. Koichi Koganezawa and N. Shimizu, "Antagonistic muscle-like actuator and its application to multi-d.o.f. forearm prosthesis," *Advanced Robotics*, vol. 12, no. 7-8, pp. 771–789, 1997.

[15] M. Lauria, M.-A. Legault, M.-A. Lavoie, and F. Michaud, "High performance differential elastic actuator for robotic interaction tasks," in *Multidisciplinary Collaboration for Socially Assistive Robotics*, AAAI Spring Symposium, 2007, pp. 39–41.

[16] C. Lee and S. Oh, "Configuration and performance analysis of a compact planetary geared Elastic Actuator," in *Annual Conference of the IEEE Industrial Electronics Society (IECON)*, 2016, pp. 6391–6396.

[17] A. Kakogawa and S. Ma, "A Differential Elastic Joint for Multi-linked Pipeline Inspection Robots,"

in *IEEE/RSJ International Conference on Intelligent Robots and Systems (IROS)*, 2018, pp. 949–954.

[18] P. Herodotou and S. Wang, "Design, modelling, and experimental evaluation of a compact elastic actuator for a gait assisting exoskeleton," in *IEEE International Conference on Rehabilitation Robotics (ICORR)*, 2019, pp. 331–336.

[19] D. Cheon, K. Nam, and S. Oh, "Design and robust control of a precise torque controllable steering module for steer-by-wire systems," *IEEE Transactions on Industrial Electronics (TIE)*, vol. 69, no. 12, pp. 13 245–13 254, 2022.

[20] M. Hutter, "StarlETH & Co.: Design and control of legged robots with compliant actuation," Ph.D. dissertation, ETH Zurich, 2013.

[21] F. Negrello, M. Garabini, M. G. Catalano, *et al.*, "A modular compliant actuator for emerging high performance and fall-resilient humanoids," in *IEEE/RAS International Conference on Humanoid Robots (Humanoids)*, 2015, pp. 414–420.

[22] S. Haddadin, T. Laue, U. Frese, S. Wolf, A. Albu-Schäffer, and G. Hirzinger, "Kick it with elasticity: Safety and performance in human-robot soccer," *Robotics and Autonomous Systems*, vol. 57, no. 8, pp. 761–775, 2009.

[23] H. Goya, K. Matsusaka, M. Uemura, Y. Nishioka, and S. Kawamura, "Realization of high-energy efficient pick-and-place tasks of scara robots by resonance," in *IEEE/RSJ International Conference on Intelligent Robots and Systems (IROS)*, 2012, pp. 2730–2735.

[24] D. F. B. Haeufle, M. D. Taylor, S. Schmitt, and H. Geyer, "A clutched parallel elastic actuator concept: Towards energy efficient powered legs in prosthetics and robotics," in *IEEE/RAS/EMBS International Conference on Biomedical Robotics and Biomechatronics (BioRob)*, 2012, pp. 1614–1619.

[25] B. Penzlin, M. Enes Fincan, Y. Li, L. Ji, S. Leonhardt, and C. Ngo, "Design and analysis of a clutched parallel elastic actuator," *Actuators*, vol. 8, no. 3, 2019.

[26] J. Reinecke, B. Deutschmann, A. Dietrich, and M. Hutter, "An anthropomorphic robust robotic torso for ventral/dorsal and lateral motion with weight compensation," *IEEE Robotics and Automation Letters (RA-L)*, IEEE, vol. 5, no. 3, pp. 3876–3883, 2020.

[27] F. Ostyn, B. Vanderborght, and G. Crevecoeur, "Overload clutch with integrated torque sensing and decoupling detection for collision tolerant hybrid high-speed industrial cobots," *IEEE Robotics and Automation Letters (RA-L)*, vol. 7, no. 4, pp. 12 601–12 607, 2022.

[28] M. Plooij, M. Wisse, and H. Vallery, "Reducing the energy consumption of robots using the bidirectional clutched parallel elastic actuator," *IEEE Transactions on Robotics (T-RO)*, vol. 32, no. 6, pp. 1512–1523, 2016.

[29] W. Roozing, J. Malzahn, N. Kashiri, D. G. Caldwell, and N. G. Tsagarakis, "On the stiffness selection for torque-controlled series-elastic actuators," *IEEE Robotics and Automation Letters (RA-L)*, vol. 2, no. 4, pp. 2255–2262, 2017.

[30] C. English and D. Russell, "Implementation of variable joint stiffness through antagonistic actuation using rolamite springs," *Mechanism and Machine Theory*, vol. 34, pp. 27–40, 1 1999.

[31] G. Tonietti, R. Schiavi, and A. Bicchi, "Design and control of a variable stiffness actuator for safe and fast physical human/robot interaction," in *IEEE International Conference on Robotics and Automation (ICRA)*, 2005, pp. 526–531.

[32] R. Schiavi, G. Grioli, S. Sen, and A. Bicchi, "VSA-II: A novel prototype of variable stiffness actuator for safe and performing robots interacting with humans," in *IEEE International Conference on Robotics and Automation (ICRA)*, 2008, pp. 2171–2176.

[33] F. Petit, W. Friedl, H. Höppner, and M. Grebenstein, "Analysis and synthesis of the bidirectional antagonistic variable stiffness mechanism," *IEEE/ASME Transactions on Mechatronics (TMECH)*, vol. 20, no. 2, pp. 684–695, 2015.

[34] A. Jafari, N. G. Tsagarakis, and D. G. Caldwell, "AwAS-II: A new actuator with adjustable stiffness based on the novel principle of adaptable pivot point and variable lever ratio," in *IEEE International Conference on Robotics and Automation (ICRA)*, 2011, pp. 4638–4643.

[35] B. Vanderborght, N. G. Tsagarakis, R. Van Ham, I. Thorson, and D. G. Caldwell, "MACCEPA 2.0: Compliant actuator used for energy efficient hopping robot Chobino1D," *Autonomous Robots*, vol. 31, pp. 55–65, 2011.

[36] S. Groothuis, G. Rusticelli, A. Zucchelli, S. Stramigioli, and R. Carloni, "The vsaUT-II: A novel rotational variable stiffness actuator," in *IEEE International Conference on Robotics and Automation (ICRA)*, 2012, pp. 3355–3360.

[37] S. Wolf and J.-E. Feenders, "Modeling and benchmarking energy efficiency of variable stiffness actuators on the example of the DLR FSJ," in *IEEE/RSJ International Conference on Intelligent Robots and Systems (IROS)*, 2016, pp. 529–536.

[38] S. Wolf and G. Hirzinger, "A new variable stiffness design: Matching requirements of the next robot generation," in *IEEE International Conference on Robotics and Automation (ICRA)*, 2008, pp. 1741–1746.

[39] O. Eiberger, S. Haddadin, M. Weis, A. Albu-Schäffer, and G. Hirzinger, "On joint design with intrinsic variable compliance: Derivation of the DLR QA-Joint," in *IEEE International Conference on Robotics and Automation (ICRA)*, 2010, pp. 1687–1694.

[40] N.-D. Vuong, R. Li, C.-M. Chew, A. Jafari, and J. Polden, "A novel variable stiffness mechanism with linear spring characteristic for machining operations," *Robotica*, vol. 35, no. 7, pp. 1627–1637, 2017.

[41] J. Reinecke, A. Dietrich, A. Shu, B. Deutschmann, and M. Hutter, "A robotic torso joint with adjustable linear spring mechanism for natural dynamic motions in a differential-elastic arrangement," *IEEE Robotics and Automation Letters (RA-L)*, vol. 7, no. 1, pp. 9–16, 2022.

[42] C. W. Mathews and D. J. Braun, "Design of parallel variable stiffness actuators," *IEEE Transactions on Robotics (T-RO)*, vol. 39, no. 1, pp. 768–782, 2023.

[43] M. J. Kim, A. Werner, F. C. Loeffl, and C. Ott, "Enhancing joint torque control of series elastic actuators with physical damping," in *IEEE International Conference on Robotics and Automation (ICRA)*, 2017, pp. 1227–1234.

[44] S. Monteleone, F. Negrello, M. G. Catalano, M. Garabini, and G. Grioli, "Damping in compliant actuation: A review," *IEEE Robotics & Automation Magazine*, vol. 29, no. 3, pp. 47–66, 2022.

[45] S. Monteleone, F. Negrello, G. Grioli, and M. G. Catalano, "dSEDA: A differential series elastic damped actuator," in *IEEE International Conference on Robotics and Automation (ICRA)*, 2022, pp. 11 395–11 401.

[46] C. Lee, S. Kwak, J. Kwak, and S. Oh, "Generalization of series elastic actuator configurations and dynamic behavior comparison," *Actuators*, vol. 6, no. 3, 2017.

[47] H. W. Müller, *Die Umlaufgetriebe* (Konstruktionsbücher). Springer Berlin Heidelberg, 1998, vol. 28.

[48] C. Lee, D. Cheon, and S. Oh, "High fidelity impedance control of series elastic actuator for physical human-machine interaction," in *Annual Conference of the IEEE Industrial Electronics Society (IECON)*, vol. 1, 2019, pp. 3621–3626.

[49] W. J. Stronge, *Impact Mechanics*, 2nd ed. Cambridge University Press, 2018.

[50] J. R. Barber, "Impact," in *Contact Mechanics*. Springer International Publishing, 2018, pp. 513–541.

[51] Y. Wang, N. Dehio, and A. Kheddar, "On inverse inertia matrix and contact-force model for robotic manipulators at normal impacts," *IEEE Robotics and Automation Letters (RA-L)*, vol. 7, no. 2, pp. 3648–3655, 2022.

[52] Harmonic Drive SE. "Harmonic drive® gears, Gear component sets." (2022), [Online]. Available: https://harmonicdrive.de/fileadmin/user_upload/Harmonic_Drive_Gears_EN_1050860_06_2022.pdf (visited on 03/30/2023).

[53] P. M. Wensing, A. Wang, S. Seok, D. Otten, J. Lang, and S. Kim, "Proprioceptive actuator design in the MIT Cheetah: Impact mitigation and high-bandwidth physical interaction for dynamic legged robots," *IEEE Transactions on Robotics (T-RO)*, vol. 33, no. 3, pp. 509–522, 2017.

[54] K. Kojima, Y. Kojio, T. Ishikawa, *et al.*, "Drive-train design in JAXON3-P and realization of jump motions: Impact mitigation and force control performance for dynamic motions," in *IEEE/RSJ International Conference on Intelligent Robots and Systems (IROS)*, 2020, pp. 3747–3753.

[55] M. Iskandar, C. Ott, O. Eiberger, M. Keppler, A. Albu-Schäffer, and A. Dietrich, "Joint-level control of the dlr lightweight robot sara," in *IEEE/RSJ International Conference on Intelligent Robots and Systems (IROS)*, 2020, pp. 8903–8910.

[56] M. Waszak and J. Fung, "Parameter estimation and analysis of actuators for the BACT wind-tunnel model," in *Atmospheric Flight Mechanics Conference*, AIAA, 1996, pp. 22–30.

[57] G. Goertzel, "An algorithm for the evaluation of finite trigonometric series," *The American Mathematical Monthly*, vol. 65, no. 1, pp. 34–35, 1958.

[58] L. Le Tien, A. Albu-Schäffer, A. De Luca, and G. Hirzinger, "Friction observer and compensation for control of robots with joint torque measurement," in *IEEE/RSJ International Conference on Intelligent Robots and Systems (IROS)*, 2008, pp. 3789–3795.

[59] M. Keppler, D. Lakatos, C. Ott, and A. Albu-Schäffer, "Elastic structure preserving impedance (ESπ) control for compliantly actuated robots," in *IEEE/RSJ International Conference on Intelligent Robots and Systems (IROS)*, 2018, pp. 5861–5868.

[60] M. Keppler, D. Lakatos, C. Ott, and A. Albu-Schäffer, "A passivity-based approach for trajectory tracking and link-side damping of compliantly actuated robots," in *IEEE International Conference on Robotics and Automation (ICRA)*, 2016, pp. 1079–1086.

[61] A. Albu-Schäffer, C. Ott, and G. Hirzinger, "A unified passivity-based control framework for position, torque and impedance control of flexible joint robots," *The International Journal of Robotics Research (IJRR)*, vol. 26, no. 1, pp. 23–39, 2007.

[62] S. Wolf and A. Albu-Schaffer, "Towards a robust variable stiffness actuator," in *IEEE/RSJ International Conference on Intelligent Robots and Systems (IROS)*, 2013, pp. 5410–5417.

[63] I. Walker, "Impact configurations and measures for kinematically redundant and multiple armed robot systems," *IEEE Transactions on Robotics and Automation*, vol. 10, no. 5, pp. 670–683, 1994.

[64] B. R. So, J. H. Lee, B.-J. Yi, and W. Kim, "Robot motion generation considering external and internal impulses," in *IEEE/RSJ International Conference on Intelligent Robots and Systems (IROS)*, 2005, pp. 948–953.

[65] J.-J. Park, J.-B. Song, and S. Haddadin, "Collision analysis and safety evaluation using a collision model for the frontal robot–human impact," *Robotica*, vol. 33, no. 7, pp. 1536–1550, 2015.

Anton Shu holds a B.Sc. in Mechatronics and Information Technology from the Technical University of Munich, Germany, awarded in 2014, and an M.Sc. in Mechanical Engineering from the same institution, awarded in 2018. He has been with the German Aerospace Center (DLR), Institute of Robotics and Mechatronics, Wessling, Germany, since that time. His research interest lies in the development of actuation systems for large legged robotic systems, with a particular focus on quadrupeds and humanoids.

Clara Raschel received the B.Sc. degree in Mechanical Engineering in 2019 and the M.Sc. degree in Robotics, Cognition, Intelligence in 2022 from the Technical University of Munich, Germany. Since then, she has been with the German Aerospace Center (DLR), Institute of Robotics and Mechatronics, Wessling, Germany. Her current research interests include modeling and control of flexible joint robots, impedance control, energy efficiency and positioning accuracy.

Manuel Keppler received his B.S. in Molecular Biology from the University of Vienna in 2009 and his B.S. and M.S. in Mechanical Engineering from the Technical University of Vienna in 2012 and 2014. He earned his Ph.D. in Computer Science from the Technical University of Munich in 2023. Dr. Keppler joined the DLR Institute of Robotics and Mechatronics in 2014 as a research scientist. Since 2019, he has led control developments for the wheeled humanoid DLR David. From 2019 to 2020, he was a Visiting Researcher at Sapienza University in Rome, and since 2023, he leads the Elastic Robot Control group at DLR. His team advances robot control, planning, and design for elastic robots to achieve human-like motion performance. He is an Associate Editor for IEEE Robotics and Automation Letters and served as General Co-chair for the 2023 International Workshop on Human-Friendly Robotics. He is the General Co-chair for the 2024 RSS Pioneers. Dr. Keppler has received several awards, including the Best Automation Paper Award Finalist at the 2016 IEEE International Conference on Robotics and Automation, an IEEE Robotics and Automation Letters Best Paper Award Honorable Mention in 2023, and the George Giralt PhD Award in 2024.

Armin Wedler is Head of Planetary Exploration at DLR Institute of Robotics and Mechatronics, studied mechanical engineering and robotics and has a doctorate on ”Adaptive passive compliant systems for use in robotics” in 2010 from the University of Hannover. He works at DLR since 2008. Within his work, Mr. Wedler aims to support sustainable technologies for humanity, including the use of robots in crisis regions, food supply chains and agriculture to combat climate change and improve food production. With the coordination of the AHEAD (autonomous humanitarian emergency aid devices) Project within (DLR). At the HGF funded iFOODis project (2023-2027), he will focus the work on intelligent robotic systems to increase sustainability of food cycles.

Martin Görner received his M.S. in mechanical engineering from Rose-Hulman Institute of Technology, Terre Haute, USA in 2005, his Dipl.-Ing. degree in mechatronics engineering from the Otto-von-Guericke University, Magdeburg, Germany in 2007 and his Dr.-Ing. for his work on “Locomotion and Pose Estimation in Compliant, Torque-Controlled Hexapedal Robots” from TU Ilmenau, Germany, in 2017. Since 2007 he is with the Institute of Robotics and Mechatronics of the German Aerospace Center in Wessling, Germany. His research interests include the mechatronics and control of legged and wheeled mobile robots with applications to planetary exploration and the factory of the future. Currently, he is responsible for the new Moon-Mars test site of the institute as well as the systems engineering of LUNA TRP – a new hybrid legged-wheeled rover platform.